Cancerous Inhibitor of Protein Phosphatase 2A (CIP2A) modifies energy metabolism via 5' AMP-activated protein kinase signalling in malignant cells

James A Austin[1], Rosalind E Jenkins[2], Gemma M Austin[1], Mark A Glenn[1], Karen Dunn[1], Laura Scott[1], Claire M Lucas[1,3], Richard E Clark[1]

[1]Department of Molecular and Clinical Cancer Medicine, Institute of Translational Medicine, University of Liverpool, UK.
[2]Department of Molecular and Clinical Pharmacology, Institute of Translational Medicine, University of Liverpool, UK.
[3] Faculty of Medicine, Dentistry and Life Sciences, Chester Medical School, University of Chester, UK.

Corresponding Author: Dr. James A. Austin
Department of Molecular and Clinical Cancer Medicine,
University of Liverpool,
Ashton Street,
Liverpool L69 3GE
United Kingdom
Email: JAustin@Liverpool.ac.uk
Telephone: +44 (0)151-79-49586
Mobile: +44 (0)7837185767

Running title: CIP2A modifies energy metabolism via AMPK (41 characters inc. spaces)

Format: Research Article;

Word counts: Title: 19 words, Abstract 185 words; Main text 6052 words (including all text except abstract, title page, figure/table legends and references).
6 Figures, 1 Supplementary Table, 55 references.

Disclosure of potential conflict of interest: The authors declare no potential conflicts of interest.

Funding: No specific funding received.

ABSTRACT

Cancerous Inhibitor of protein phosphatase 2A (CIP2A) is an adverse biomarker across many malignancies. Using K562 cells engineered to have high or low CIP2A expression, we show that high CIP2A levels significantly bias cellular energy production towards oxidative phosphorylation (OXPHOS) rather than glycolysis. Mass spectrometric analysis of CIP2A interactors and isobaric tagging for relative and absolute protein quantitation (ITRAQ) experiments identified many associated proteins, several of which co-vary with CIP2A level. Many of these CIP2A associating and co-varying proteins are involved in energy metabolism including OXPHOS, or in 5' AMP-activated protein kinase (AMPK) signalling, and manipulating AMPK activity mimics the effects of low/high CIP2A on OXPHOS. These effects are dependent on the availability of nutrients, driven by metabolic changes caused by CIP2A. CIP2A level did not affect starvation induced AMPK phosphorylation of Unc-51 autophagy activating kinase 1 (ULK-1) at Ser555, but autophagy activity correlated with an increase of AMPK activity, to suggest that some AMPK processes are uncoupled by CIP2A, likely via its inhibition of protein phosphatase 2A (PP2A). The data demonstrate that AMPK mediates this novel CIP2A effect on energy generation in malignant cells.

SIGNIFICANCE

High levels of CIP2A are associated with poor clinical outcome in at least 20 different malignancies, making it an attractive therapeutic target. CIP2A inhibits PP2A and stabilises MYC. We show a novel association between CIP2A and OXPHOS, via AMPK signalling, suggesting a new therapeutic network to overcome CIP2A-mediated poor prognosis.

Keywords: Cancerous inhibitor of protein phosphatase 2A, CIP2A, protein phosphatase 2A, PP2A, 5' AMP-activated protein kinase, AMPK, leukaemia, cancer, oxidative phosphorylation, OXPHOS

INTRODUCTION

Protein phosphatase 2A (PP2A) is an abundant cellular phosphatase. It is central to reversing substrate phosphorylation caused by the overactive kinase events that characterise most human malignancies. Many of these inappropriately phosphorylated substrates contribute to deranged cellular processes that contribute to the malignant phenotype. PP2A is thus an important tumour suppressor.

Phosphorylation of PP2A at tyrosine residue 307 (P-Tyr-307-PP2A) leads to PP2A inactivation. PP2A is suppressed in many human malignancies; indeed malignant transformation may require suppression of PP2A activity [1]. PP2A suppression in malignancy is almost entirely due to its natural inhibitors. Of these, cancerous inhibitor of PP2A (CIP2A) has emerged as an important oncogene since its discovery [2] and the recognition of its interaction with PP2A by Westermarck and colleagues [3]. To date, over 220 papers have been published on the clinical consequences of high CIP2A levels in malignancies, and all associate higher levels with a poor outcome, adverse histology and/or a poor response to treatment (meta-analysis by Tang et al 2018 [4]), in both common and rarer epithelial tumour types, and in chronic [5,6] and acute [7] myeloid leukaemias.

In contrast to this breadth of clinical correlative information, little is known of CIP2A's mechanism of action. A direct interaction between CIP2A and PP2A has been described, showing CIP2A binds at least two PP2A regulatory subunits, specifically β56γ and β56α [8]. The structure of the N-terminal region (residues 1-560) of CIP2A has been determined. This region is important in facilitating PP2A binding, as it contains the homodimer contacts, spanning residues 507-559 that enhance CIP2A's binding to PP2A subunits. The minimum region required for CIP2A binding to β56α and β56γ has been identified as residues 159-245 [8]; however a structure containing both CIP2A and PP2A components has yet to be identified. Whether these interactions fulfil all CIP2A binding are unknown as despite efforts by us and others, the full length protein is unstable and has not yielded any crystals for X-ray crystallographic structural study.

In CIP2A immunoprecipitation experiments from Hela cells, CIP2A associates with MYC [3]. This interaction is direct and involves the N-terminal residues 1-262 of MYC. CIP2A level enhances MYC expression and activation (indicated by phosphorylation on serine 62 (P-Ser-62-MYC)) and MYC localisation to nuclear lamins in cancer cell lines [9-11]. The mechanism for CIP2A's regulation on MYC is likely through its inhibitory effect on PP2A-mediated MYC dephosphorylation (which inactivates MYC and decreases its stability). However, the possibility that CIP2A may also have additional actions has not been examined. Using the chronic myeloid leukaemia (CML) cell line K562 engineered to have either high or low levels of CIP2A, we here present evidence that CIP2A augments oxidative phosphorylation (OXPHOS) and decreases reliance on glycolysis. Also, CIP2A directly interacts with a number of proteins that are involved in energy metabolism in a manner suggesting that these metabolic effects are mediated through 5' adenosine monophosphate-activated protein kinase (AMPK), and this is supported by the observation that modifying AMPK activity mimics the effects of CIP2A on energy metabolism. These findings constitute a novel mechanism of action for CIP2A in malignancy.

MATERIALS AND METHODS

K562 fractionation and western blots

K562 lysates were prepared in RIPA buffer containing halt™ protease inhibitor (ThermoFisher Scientific, Loughborough, Leicestershire, UK) and 2mM phosphatase inhibitor (2mM $NaVO_4$ Sigma-Aldrich, Gillingham, Dorset, UK). Cell lysis was achieved by sonication and the supernatant was collected after removing cell debris by centrifugation at 16,000g at 4°C. Supernatants were quantified by DC™ protein determination kit (Bio-Rad, Watford, Hertfordshire, UK) and loaded at 20µg per well for western blot analysis. CIP2A components were probed using antibodies for CIP2A (Santa Cruz, Dallas, Texas, US), PP2A C (Millipore, Watford, Hertfordshire, UK), PP2A C (recognising P-Tyr-307-PP2A) (Santa Cruz), MYC (Santa Cruz) and P-Ser-62-MYC (Abcam, Milton, Cambridgeshire, UK). Kaleidoscope™ molecular weight markers (Bio-Rad) were used to estimate molecular masses, and shown relative to the target of interest in kDa as indicated. Nuclear and cytoplasmic fractionation was achieved as described in the NE-PER Nuclear and Cytoplasmic reagent kit protocol (ThermoFisher Scientific). The control and secondary antibodies used were Poly (ADP-ribose) polymerase (PARP, Abcam), β-actin (Sigma-Aldrich) and conjugate horseradish peroxidase containing antibodies raised against mouse or rabbit (Cell Signalling Technologies, Danvers, Massachusetts, U.S.) respectively. The AMPK and P-Thr-172 AMPK antibodies used for assessing the AMPK signalling components and glucose transporter type 4 (GLUT4) were all from Cell Signalling Technologies. To quantitate autophagy, antibodies from Cell Signalling Technologies were used to assess relative levels of the AMPK target, Unc-51 like autophagy activating kinase 1 (ULK-1), phosphorylated at Ser 555 and the autophagy marker, microtubule-associated protein 1A/1B light chain 3, isoform B, recognising both cytosolic (LC3I) and autophagosome associated form (LC3II). Drug treatments 5-aminoimidazole-4-carboxamide

ribonucleotide (AICAR) (Abcam), A-769662 (Abcam), Compound C (Abcam) and okadaic acid (Cayman Chemical Company, Ann Arbor, Michigan, U.S.) were included at the final concentrations and incubation times stated, at $5x10^5$/ml cell density.

Low and high fed conditions

To generate low and high nutrient conditions, the CIP2A modified cell lines were fed at a cell density of $1x10^6$ cells/ml in RPMI with phenol red pH indicator included (Sigma-Aldrich), supplemented with 2mM L-glutamine (ThermoFisher Scientific) and 100 U/0.1mg/ml penicillin streptomycin (ThermoFisher Scientific) and left for 3 days at 37°C in a CO_2 incubator. The colour of the media changed to yellow, indicating a reduction in pH by the phenol indicator. Lysates were then collected for starved cells as previously described. For fed conditions, starved cells were fed in the fresh media at a cell density of $1x10^6$ cells/ml and left for 24 hours as similarly described with no noticeable change to the colouration of the media.

Generation of CIP2A modified cell lines and Lentiviral Vector Design

The CIP2A (accession number: NM_020890) coding sequence was amplified from a CIP2A plasmid (NM_020890) human tagged ORF clone (Origene, Wembley, Middlesex, UK) and K562 DNA respectively, with necessary recombination sequences and transferred into a pLNT transfer vector for CIP2A+ and CIP2A- respectively using standard Gateway calking protocols. CIP2A destination vectors were then separately cloned into a venus C-fusion lentiviral vector (pLNT-UbC-#-venus) for either CIP2A+, generously donated by Prof. Mike White at the University of Manchester, UK or in psPAX2 for the generation of CIP2A-. The propagation and cloning of the lentiviral vectors and lentivirus production using HEK293T cells and subsequent transfection of K562 cells were performed as described for CIP2A+ [12] and for CIP2A- [13]. The cell lines generated were derived from a single transfection.

Flow cytometry and determination of cellular size, proliferation and survival.

Cellular sizes, proliferation and annexin V/propidium iodide (PI) survival assays were all performed on the Attune NxT flow cytometer (ThermoFisher Scientific). Flow speeds were set at 100ul/min and voltage settings were consistent between all cell lines in each respective experiment.

Changes in cell size between CIP2A modified cell lines were assessed by comparing differences between side and forward scatter profiles of the main cell population. The geometric mean for the forward scatter and count was taken and overlaid as histograms, constructed using Flojo™ version 10 software (BD, Ashland, Oregon, US). Proliferation was assessed by comparing the fluorescent decline of carboxyfluorescein succinimidyl ester (CFSE), caused by dividing cells and dilution of the signal over 0h, 14h, 24h, 48h, 72h and 84h timepoints. Briefly, cells were washed in PBS, treated with Far-red CFSE (ThermoFisher Scientific) at a final concentration of 0.5μM and incubated at 37°C for 30 minutes, protected from light and shaken every 5 minutes throughout this period. CFSE was removed by centrifugating cells at 500g and removing media. Cell pellets were washed in RPMI, rested for 15 minutes in a CO_2 incubator set at 37°C and similarly washed twice more in complete RPMI media. Untreated and CFSE treated cell populations were then measured by flow cytometry, using red-laser1 (RL1) at the times specified.

Cell survival was tested in both high and low nutrient conditions. Annexin V binding buffer (10mM HEPES, 150Mm NaCl and 2.5mM CaCl2, made in PBS at pH 7.4) including 5% of Alexa fluor 647 annexin V (Biolegends, San Diego, California, US) was added to achieve a 50% mix. Immediately before flow cytometry assessment, 2μl of a 1:20 dilution of PI (Sigma-Aldrich) was added to the mix, shaken and the blue laser3 and RL1 were used to detect the fluorescence emitted from PI and Alexa fluor 647 annexin V respectively. Viable, early and

late apoptotic populations (annexin V -/PI-, annexin V+/PI- and annexin V +/PI+ respectively) were assessed using the Attune NxT software (ThermoFisher Scientific).

Experiments were repeated 3 times for each cell line in all flow cytometry experiments. Statistical analysis was carried out using Graphpad Prism version 7 (GraphPad, La Jolla, California, US) and unpaired Student's T-test.

Seahorse Metabolic Assays

All seahorse consumables were purchased from Agilent (Agilent, Cheadle, Greater Manchester, UK). XF96 cell culture microplates (Agilent) were pre-treated with 10µl of 22µg/ml cell-tak™ solution (ThermoFisher Scientific), in 0.1M bicarbonate buffer at pH 8 the previous day, as described in the manufacturers' protocol. Each K562 cell line was washed and suspended in unbuffered Seahorse XF base media (Agilent), containing 1mM sodium pyruvate and 2mM L-glutamine at pH 7.4. D-glucose at 25mM was added for mitochondrial stress testing. A total of 70,000 cells from each K562 cell line were added per well, and attached by centrifugation at 50g over 5 minutes, with minimum accelerating and decelerating speeds set, then settled at 37°C in a CO_2-free incubator for at least 30 minutes prior to seahorse analysis.

The XF injection plate for the mitochondrial stress test was set up to dispense 25µl for final concentrations of 1.5µM oligomycin A, 0.75µM carbonyl cyanide-4-(trifluoromethoxy)phenylhydrazone (FCCP) and 1µM each of rotenone and antimycin A. For the glycolysis stress test, 10mM D-glucose, 1.5µM oligomycin A and 100µM 2-deoxy-D-glucose were used. Experiments were run over 75 minutes using Seahorse XF96 instrumentation (Agilent). Three replicates for each stress test were performed, with each containing at least 3 technical replicates to construct an averaged profile for each of the 3 K562 cell lines. Data were analysed using Wave 2.4 (Agilent) and normalised to non-glycolytic acidification at the final point before the addition of glucose or to non-mitochondrial respiration respectively. Mitochondrial stress tests adapted to incorporate AMPK modifying compounds, 4mM AICAR (Abcam) and 10µM Compound C (Abcam) were run as described with an extra stage measuring each compound's effect after initial basal measurement over the course of an hour, compared against initial basal rate or relative vehicle control as specified. Column plots were constructed using with standard error using Graphpad Prism Version 7 (GraphPad, La Jolla, California, US) and unpaired Student's T-test with Welch correction was used for statistical analysis.

Protein Extraction and ITRAQ labelling

A total of $1x10^8$ cells from each K562 derived cell line were twice washed in PBS then resuspended and lysed in 0.5M triethylammonium bicarbonate (TEAB) (Sigma-Aldrich) and 1% sodium dodecyl sulphate (SDS) (Sigma-Aldrich) at 4°C. Concentrated Halt™ protease and phosphatase inhibitors were then added to achieve the recommended 1x working concentration (ThermoFisher Scientific). Prior to isobaric tagging for relative and absolute protein quantitation (ITRAQ), samples were diluted 10-fold in 0.5M TEAB, to reduce protease inhibitor concentration and allow for overnight trypsin digestion. The final protein concentrations were made to 100µg protein in 20µl volume, as determined by Bradford assay [14] (ThermoFisher Scientific). Labelling for the 8plex ITRAQ methodology was according to the SCIEX protocol as used previously [15]. Briefly, protein lysates were reduced in 1mM tris(2-carboxyethyl)phosphine (TCEP) (ThermoFisher Scientific), and self-linking cysteine residues capped by treatment with 10mM methyl methanethiosulfate (MMTS) agent (ThermoFisher Scientific) before overnight trypsin digestion, using trypsin gold™ graded for MS use (Promega, Madison, Wisconsin, US). The trypsinised protein samples were then labelled with 8plex ITRAQ tagging reagents, using all available mass labels, ranging from 113-121 (SCIEX, Framingham, Massachusetts, US). Samples were brought to pH 3 with phosphoric acid and the complex protein mixture was cleaned and fractionated by strong-cation exchange chromatography (Polysulfoethyl A column 200 x 4.6mm, 5µm, 300Å; Poly LC, Columbia, Maryland, US). 2ml fractions containing protein

were dried under vacuum (SpeedVac, Eppendorf, Stevenage, UK) and reconstituted in 1ml 0.1% trifluoroacetic acid (Sigma-Aldrich) before desalting on a mRP Hi Recovery column (4.6 x 50mm, Agilent) using an Agilent 1260 HPLC system (Agilent).

Mass spectrometry setup and parameters

Desalted fractions were reconstituted into 40µl of 0.1% formic acid (Sigma-Aldrich) and delivered into a TripleTOF 6600 system (SCIEX) in 5µl aliquots via an Eksigent NanoLC 400 system (SCIEX) mounted with a NanoAcquity (5µm, 180µm x 20mm) C_{18} trap and analytical column (1.7µm, 75µm x 250mm, Waters, Wilmslow, Cheshire, UK). A NanoSpray III source was fitted with a 10µm inner-diameter PicoTip emitter (New Objective, Woburn, Massachusetts, US). A gradient from 2-50% acetonitrile/ 0.1% formic acid was applied over 90 minutes at 0.3µl/min. Peptide spectra were acquired in positive ion mode using information-dependent acquisition by the Analyst TF1.7 software (SCIEX), with survey scans of 250ms. The MS/MS accumulation time was set for 100ms with monitoring of the 25 most intense ions (total cycle time 2.75s).

Mass spectrometry data processing

Data were searched using ProteinPilot5 software (SCIEX) against the UniProt database (release-2017_03, 20 201 human proteins), set to incorporate ITRAQ and MMTS as modifications. Data were also searched against a reverse database, to eliminate proteins that lay outside the 1% false discovery rate limit. A total of 6 biological repeats were obtained from merging four ITRAQ experiments. The experiments were performed as two sets of two 8plex experiments with a reference pool shared between pairs. The merged data were reduced to contain proteins identified by at least 1 peptide at 99% confidence or 2 peptides at 90%. These data were Log2 transformed and processed using the batch-correction feature of Partek genomic suite 7 (Partek Genomic Suite software, v. 7.18.0518, St. Louis, Missouri, US) to eliminate pool and ITRAQ experiment biases. Protein changes between cell lines were tested using these data and an ANOVA analysis was utilised to identify differences between cell types. As a precaution, the data prior to batch correction were also tested using an ANOVA with these factors included as variables, and proteins not present in both sets of analysis were removed. Principal component analysis (PCA) was performed using Partek genomic suite on these batch-corrected data. The heatmap showing significant changes ($p<0.05$) by ANOVA between CIP2A+ and CIP2A- was Zscored with incomplete datasets removed prior to analysis by Perseus Proteomic Software suite (Max Planck Institute, Munich, Germany) [16]. The heatmap was constructed using Euclidean linkages to sort both row and column values with default settings applied. Pathway analyses were performed using DAVIDdb [17,18].

Immunoprecipitations and CIP2A-venus extraction

CIP2A was isolated using immunoprecipitations (IP) on protein lysates from K562 cells. A venus fluorophore tagged version of CIP2A was also immunoprecipitated from CIP2A+ cell line protein lysates. Each isolation experiment used $1x10^8$ cells for each respective cell line. Protein lysates were prepared by sonication in 50mM Tris-HCL pH 8, 150mM NaCl, 1mM EDTA, 1mM EGTA and 0.1% Triton X100 including Halt™ protease and phosphatase inhibitors (ThermoFisher Scientific). Prior to IP, protein A/G magnetic beads (ThermoFisher Scientific) were precoated with the target's respective antibody using 20µg/50µg of bead. For CIP2A IP, two antibodies were used targeting either its N' or C'-terminal (ab128179; Abcam, & sc80660; Santa Cruz respectively) alongside a mouse control (ab18447, Abcam) performed identically. The CIP2A-venus targeted pull-down was incubated for two hours on ice and washed twice in the same buffer and extracted using 20µl GFPtrap™ beads (ChromoTek, Planegg-Martinsried, Germany).

Prior to mass spectrometry analysis, samples were washed twice more in phosphate buffer (PB) at pH 7.4, pelleted and resuspended in 100µl PB with 10mM dithiothreitol (DTT) (Sigma-Aldrich) and incubated at room temperature for 15 min. The cysteine capping reagent iodoacetamide (Sigma-Aldrich) was added to stop the reforming of disulphide

bonds, at 50mM final concentration and incubated at 15 min at room temperature. This was then washed three times in 100µL PB and resuspended in 50µl with 0.5µg trypsin (Promega) and incubated overnight at 37°C. Samples were cleaned from contaminants using C_{18} ZipTips (Millipore). A total of 2 ZipTips were used to pool 20µl from each sample. 5µl of the zip-tipped sample was analysed on a Triple TOF 6600 as described above. The resulting protein lists were further subtracted, using results obtained from an antibody control of same species or GFPtrap™ control (using only unmodified K562 lysate); both were run parallel to the IP test experiments. Data were analysed using DAVID and cytoscape with STRING app; pValues were obtained from STRING EASE scoring. Protein associations and interactions were identified and visualised using Cytoscape [19,20] and installed apps STRING [21].

RESULTS

Verification of CIP2A level in modified cell lines

To investigate the effects of CIP2A, 2 lentiviral-modified K562 cell lines were generated. These either overexpressed venus fluorophore tagged CIP2A (CIP2A+) or had CIP2A expression knocked down via shRNA (CIP2A-). The CIP2A level of each line together with unmodified K562 cells was validated by western blot, shown in Figure 1A, which demonstrates a knock-down efficiency of over 98% in the CIP2A- line and an extra band corresponding to the expected molecular weight of the CIP2A-venus tagged construct in the CIP2A+ cell line. A correlation was observed between the CIP2A level and active MYC (P-Ser-62-MYC), along with an increase in inactive PP2A (P-Tyr-307-PP2A, Figure 1A), confirming that CIP2A is in an active conformation in these cells and consistent with other reports [3,5]. CIP2A was predominantly located in the cytoplasm together with PP2A, whereas MYC was mostly expressed in the nuclear compartment and this was similar for all cell lines (Figure 1B), suggesting that CIP2A activity resides within the cytoplasm and consistent with findings in other cancers [22,23].

Figure 1C demonstrates that there was no difference in cell size, assessed cytometrically by forward and side light scatter, between unmodified and CIP2A+ or CIP2A- cell lines; furthermore this was consistent in both high and low nutrient conditions. Similarly, Figure 1D shows no difference between the lines in cell viability and apoptosis rate, with each cell line in low nutrient conditions remaining at least 85% viable and less than 5% and 6% undergoing early and late apoptosis respectively. Proliferation rates were also assessed by the decay rate of a CFSE signal due to cell division, and again no differences between the cell lines were observed (all comparisons $p>0.3$, Student's T-test (data not shown). Modifying the CIP2A level therefore does not alter cell size, viability or proliferation rates.

CIP2A increases mitochondrial respiration without compromising glycolytic processes

To explore the impact of CIP2A on energy metabolism, seahorse energy metabolic stress assays were carried out using these CIP2A modified K562 cells, together with unmodified cells. Glycolysis was assessed by the extracellular acidification rate (ECAR) mainly resulting from lactate production, and mitochondrial OXPHOS by the oxygen consumption rate (OCR) driven by the components of the electron transport chain. A variety of compounds were used to manipulate these processes, as shown schematically in Figure 2A and 2E and described in their legend.

Figure 2A-2D show that reliance on glycolysis differs according to CIP2A level. The basal rate of glycolysis, in the presence of glucose, was significantly lower in CIP2A+ cells than in either CIP2A- or unmodified cells ($p < 0.0001$; Figure 2A and 2B). However, CIP2A did not impair the glycolytic machinery, since forcing cellular energy production to rely solely on glycolysis (by inhibiting mitochondrial respiration by OXPHOS with oligomycin A, an adenosine triphosphate (ATP) synthase inhibitor) allowed all cells to reach a comparable maximum rate of glycolysis (Figure 2C). A higher CIP2A level correlated with an increased

spare glycolytic capacity ($p < 0.05$; Figure 2D), thus demonstrating that CIP2A does not permanently disrupt any of the key glycolytic components and suggesting that mitochondrial activity may be higher in the CIP2A+ cell line.

The effect of CIP2A level on mitochondrial metabolism was tested in the same system, by measuring the OCR and its response to OXPHOS manipulating compounds. A higher CIP2A level correlated with an increased basal rate of OXPHOS ($p < 0.05$; Figure 2E and 2F). This increase in OXPHOS was reliant on the components of the electron transport chain, as when ATP synthase was blocked by oligomycin A, the OCR fell to a similar level irrespective of CIP2A status (Figure 2E). ATP synthase-driven ATP production was therefore more active in the high CIP2A phenotypes ($p < 0.05$; Figure 2G). The maximum rate of OXPHOS was determined by treatment with FCCP, an electron transport chain uncoupling agent; this demonstrated that the CIP2A level is significantly correlated to the maximum rate and spare capacity of OXPHOS ($p < 0.05$; Figure 2H and 2I).

CIP2A alters expression of proteins involved in energy metabolic processes, including AMPK signalling

To understand how CIP2A increases OXPHOS, differences in the proteome between each cell line were determined. The proteins from the lysate of each CIP2A-modified cell line were subjected to ITRAQ and were identified and quantified by mass spectrometry.

A total of 6 biological repeats for each cell line was performed as described over 4 8plex ITRAQ experiments. Protein levels were expressed as ratios to the reference control in each run and corrected using batch correction algorithms (Partek Genomic Suite software, v. 7.18.0518, Partek Inc. St. Louis, MO, USA) to improve comparisons between multiple runs, as similarly described [15]. A total of 229 proteins were expressed at significantly different levels between the CIP2A+ and CIP2A- cells (defined as $p < 0.05$ in ANOVA) as shown in the heat map in Figure 3A and Supplementary Table 1. These data were categorised into two datasets representing proteins over- and under-expressed with higher CIP2A, and were individually analysed for pathway enrichment in energy metabolic processes using the Database for Annotation, Visualisation and Integrated Discovery (DAVID) proteomic suite [17] and significant Fishers exact test scores (FE), ($p<0.05$). Of the 229 proteins, 27 were significantly enriched in energy metabolic pathways identified from the current Kyoto Encyclopaedia of Genes and Genomes (KEGG) database [24] (Figure 3B and C). Proteins that were upregulated with higher CIP2A levels were involved in pyruvate metabolism (FE $p = 0.0043$) and OXPHOS (FE $p = 0.024$), contributing to 3 of the 5 functional electron transport chain components (Figure 3C). This increase is consistent with the mitochondrial stress test observations of Figure 2E-2I. Similarly, the proteins downregulated with increasing CIP2A were also associated with several energy metabolic processes, including AMPK signalling (FE $p = 0.0052$).

CIP2A co-associates with proteins involved in AMPK signalling, glucose uptake and protein synthesis.

To further validate the observations from the ITRAQ proteomic analysis, proteins associating with CIP2A were identified by two techniques: by immunoprecipitation (IP) with antibodies targeting the N' or C' termini of endogenous CIP2A and by GFPtrap beads targeting the C' terminal venus fluorophore tag in the CIP2A+ cell line. For each technique, the CIP2A-associated proteins were then identified by mass spectrometry.

Results from the GFPtrap experiments identified 587 CIP2A-associated proteins, compared to 151 and 210 from the N' and C' termini targeted IPs respectively (after subtracting a non-specific antibody control), but only 52 were common to all three IPs (Figure 4A). These 52 proteins and associated interactions were visualised by the functional protein association network STRING [21] and annotated according to its databases (Figure 4B). A large proportion of these proteins shared interactions and several fell into one of 3 functional pathways as annotated in the KEGG database [24] using a modified Fischer exact

(EASE) score ($p<0.05$) in DAVID (Figure 4B). These were firstly components of the ribosome complex, involving the small 40S (RPS5, RPS27 and RPS27L) and large 60S (RPL9, RPL10 and RPL10A) subunits (EASE, $p = 0.00084$), and secondly spliceosome assembly complexes (HNRNPU, DDX39B, EIF4A3, SNRPD3, DHX15, PRPF40A) (EASE, $p = 0.00074$).

The third KEGG pathway was AMPK signalling (EASE, $p = 0.0043$), as also identified in the ITRAQ experiments. Proteins identified in this pathway included 3 members of the Rab family of G-proteins (RAB8A, RAB10 and RAB14) which are all relevant to AMPK-directed translocation of GLUT4, the activity of the platelet isoform of the key glycolytic protein, phosphofructokinase-1 (PFKP) and eukaryotic elongation factor 2 (EEF2; involved in peptide elongation during protein synthesis).

The effect of CIP2A on AMPK activity is dependent on nutrient availability

AMPK activation is demonstrated by its phosphorylation on Thr172 (P-Thr-172 AMPK), and is responsible for the majority of AMPK kinase activity [25]. P-Thr-172 AMPK activation was found to vary according to whether the availability of nutrients in the media were high (fed within the previous 24 hours after starvation) or low (fed 72 hours previously). In CIP2A- cells in low nutrient conditions, AMPK activity is higher than in high nutrient conditions, in line with the increase in the AMPK substrate GLUT4, which is normally increased by AMPK in low nutrient availability [26]. However, Figure 5A also shows that unmodified cells (which have endogenous CIP2A levels close to CIP2A+ cells as shown in Figure 1A) and CIP2A+ cells are similar in that AMPK activity is high in the high nutrient state (and higher than that in the corresponding cells in low nutrient conditions). This shows that CIP2A can disrupt normal AMPK activation conferred by low nutrient availability, whereby cells with high CIP2A have higher AMPK activity when nutrients are abundant. Furthermore, GLUT4 levels are significantly increased in both CIP2A overexpressing cells when nutrient levels are high (Figure 5A, Student's T-test $p<0.03$).

To determine whether an AMPK function other than energy metabolism also co-varied with CIP2A, phosphorylation of ULK-1 at serine 555 (P-Ser-555-ULK-1) was examined. This phosphorylation is an early step in autophagy [27, 28]. Figure 5B shows that this is only elevated in low nutrient conditions, consistent with the activation of AMPK in such conditions as seen when directly measured by P-Thr-172-AMPK in Figure 5A. However, unlike direct measurement of AMPK activity, no difference in ULK-1 levels is seen between CIP2A- and unmodified/CIP2A+ cells (Figure 5B). Autophagy was also investigated by levels of the cytosolic form of microtubule-associated protein 1A/1B-light chain 3 (LC3I) and a version of LC3I conjugated to phosphatidylethanolamine (LC3II, associated with starvation-induced autophagic activity [29]. LC3I and LC3II levels were highest in low nutrient conditions in all cell lines, consistent with higher AMPK activity in such conditions. Interestingly, Figure 5B also shows that the ratio of LC3II to LC3I, an index of autophagy [30] is significantly higher in unmodified or CIP2A+ cells than in CIP2A- cells in fed (post 24h) conditions ($p=0.05$ and 0.0224 respectively). These findings are therefore analogous to the findings of AMPK activity when measured directly by P-Thr-172-AMPK.

The effect of CIP2A on OXPHOS is mediated by AMPK activity via PP2A and independent of MYC activity.

To further investigate the effect of AMPK on metabolism, AICAR, an AMPK activator, was added to CIP2A- cells in high nutrient conditions (where AMPK activity is low as shown in Figure 5A). This significantly increased the basal rate of OXPHOS by 35% (19 pmol/min above basal, $p = 0.0368$, Student's T-test), without effect on the maximum capacity of OXPHOS (Figure 6A and 6B). Similar effects were seen with the alternative AMPK activator A-769662 at a concentration of 3 uM and 1 hour incubation (data not shown). In the converse experiment, the AMPK inhibitor Compound C was added to CIP2A+ cells in high nutrient conditions, where AMPK activity is high (as shown in Figure 5A). This significantly

reduced both basal levels and maximum rate of OXPHOS by 20% (20 pmol/min difference, p = 0.0012) and reduced the maximum capacity by half (97 pmol/min difference when normalised to each respective basal rate $p < 0.001$) respectively (Figure 6C and 6D). Figure 6A and 6C respectively show that AICAR and Compound C alter the phosphorylation status of AMPK as expected [31,32]. AMPK activity therefore affects OXPHOS, and may be an important mediator in the effect of CIP2A on energy metabolism in malignant cells.

In order to determine whether CIP2A regulation of AMPK is mediated through its known regulation on PP2A, PP2A was inhibited by addition of the phosphatase inhibitor okadaic acid in CIP2A- cells. As expected, okadaic acid decreased PP2A activity (as shown by an increased level of P-Tyr-307-PP2A) in a concentration dependent manner (Figure 5C). The inactivity of PP2A correlated with increased AMPK activity (as assessed by P-Thr-172 AMPK, showing that inhibition of PP2A by okadaic acid could mimic the changes in AMPK activity observed in the CIP2A+ cells (Figure 5A). Activation of AMPK by AICAR also had little effect on activity of P-Ser-62-MYC levels (data not shown), suggesting that MYC activity does not play a significant role in CIP2A's regulation of AMPK.

DISCUSSION

CIP2A has emerged as an important indicator of adverse outcome in cancer in the past decade, and its value as a clinically useful biomarker for individual tumour types is under investigation. At the molecular level, its interactions with PP2A and MYC have been described [3,8], but little is known of other interactions. Here we extend knowledge of the biology of CIP2A by carrying out seahorse metabolic stress assays in neoplastic cells engineered to have high or low CIP2A levels, and by mass spectrometry on ITRAQ studies and CIP2A pulldowns (both IP and tagged) in these cells. Three principal findings emerge from these studies. First, the seahorse stress assays show an increase in basal OXPHOS and a decrease in glycolysis in CIP2A+ cells. Second, proteins involved in several energy metabolic processes co-vary with CIP2A expression as revealed by ITRAQ and include those involved in not only OXPHOS but also the signalling of AMPK, an established key energy metabolism mediator. And third, manipulation of AMPK activity may modify the metabolic effects of CIP2A, through known inhibition of PP2A.

OXPHOS is a crucial cellular process, producing most of the cell's energy in the form of ATP. The observation that OXPHOS (respiration) is suppressed in malignant cells and may be accompanied by a compensatory increase in glycolysis, was made almost a century ago, and was later termed the Warburg effect after the pioneer of much of this initial work (reviewed by Liberti and Locasale [33]). Warburg proposed that this is due to dysfunctional mitochondria, and subsequent suggestions for mechanism have included imbalances in intracellular pH, defects in ATPase activity, and aberrant growth factor signalling. The increased production of lactate that results from increased glycolysis may lead to local acidosis around tumours and this may enhance tumour invasiveness [34]. However, the mechanism of the Warburg effect remains uncertain, nor is it clear whether it is a consequence of other tumour-related lesions. Here we demonstrate in a malignant cell line a phenomenon opposite to the Warburg effect, namely that high levels of CIP2A will augment OXPHOS. CIP2A has recently been reported to both suppress glycolysis in primary cilia [35], and enhance it in non-small lung cancer [36], but to the best of our knowledge it has not been reported to enhance respiration in malignancy. In fact, the Warburg effect is not universal in malignant cells; indeed early work also established that respiration is variable in tumours, and may be substantial [37], compatible with the possibility that other factors may mitigate a general Warburg effect across malignancy.

AMPK is a heterotrimeric protein, consisting of two regulatory subunits (β and γ) and a catalytic subunit; 80% of its activity is due to the α1 isoform (PRKAA1) and γ1 regulatory subunit (PRKAG1) [38]. AMPK is a master sensor of energy status [39] and becomes activated once glucose or oxygen become limited or the ADP/AMP to ATP ratio becomes

high. A key function of active AMPK is in increasing ATP-producing catabolic processes such as glucose uptake, glycolysis and OXPHOS, whilst reducing ATP usage in anabolic processes. When activated, AMPK promotes glycolysis (via activation of phosphofructokinase-2 (PFK-2) and formation of fructose-2,6-biphosphate, a potent activator of phosphofructokinase-1 (PFK-1) which is rate limiting in glycolysis [40]. Active AMPK also promotes the biosynthesis of new [41] and the disposal of dysfunctional mitochondria [42] and has been shown to induce OXPHOS function in T cell acute lymphoblastic leukaemia and electron transport chain complex I activity [43].

The present ITRAQ data show that high CIP2A is associated with lower levels of the two key AMPK components PRKAA1 and PRKAG1, and seahorse and proteomic analysis data show this is associated with reduced glycolysis. This reduced AMPK activity is also associated with a decrease in PFK-platelet type (PFKP, a component of the PFK-1 complex) to reduce glycolysis. Furthermore, high levels of CIP2A are associated with enhanced OXPHOS and an increased expression of electron transport chain components. In high CIP2A cells, two PP2A subunits were also decreased (see supplementary Table S1); the β isoform of the scaffold subunit, PPP2R1B and the α form of the β56 regulatory subunit, PPP2R5A (β56α), consistent with a reduction of PP2A activity. PP2A complexes containing the regulatory β55δ or β56γ subunits are known to directly dephosphorylate and inactivate AMPK [44-46]. In support of this, the inhibition of PP2A by okadaic acid may mimic the effect of high CIP2A, providing a potential mechanism driven by the CIP2A-PP2A interaction and regulation of AMPK activity. Nutrient availability is also a key regulator of this process, in conjunction with other studies, where CIP2A-mediated regulation of the cAMP responsive element binding protein (CREB) activity (an AMPK substrate [47,48]) was also dependent on high levels of both nutrients and CIP2A in the non-small cell lung cancer cell line H1299 [36]. Here we show that AMPK activity as measured by P-Thr-172-AMPK is elevated not only in low nutrient conditions but also in high nutrient conditions where CIP2A is also high. High CIP2A levels also modify the level of autophagy in a similar pattern when assessed by LC3II/LC3I ratio though not when assessed by serine 555 phosphorylation of ULK-1, suggesting that factors that normally mediate AMPK activity are uncoupled by CIP2A. There is evidence that AMPK can be uncoupled from autophagy events [49]. AMPK activity may also be mediated by levels of metabolites derived from metabolic pathways independent of glucose metabolism. In starved C2C12 mouse muscle cells lacking glucose and amino acids, reintroduction of free amino acids enhances the expression of P-Thr-172-AMPK, suggesting AMPK activity can be increased independently of glucose availability [50]. CIP2A has been shown to affect other anabolic processes through up-regulation of mTORC1 and MYC activity, and it is therefore plausible that changes of CIP2A level may affect local levels of amino acids and other metabolites. The present finding of AMPK activity and autophagy in relation to CIP2A may therefore be important for other effects including mitophagy, and also in other cancer types.

CIP2A may confer resistance to tyrosine kinase inhibitor therapy in CML, as previously published [5]. The present data extend those clinical findings by demonstrating a novel role for CIP2A on cellular metabolic processes, involving AMPK. This may drive several pathways conferring treatment resistance in CML, including increased OXPHOS [51], increased mTORC1 activity [52] and autophagy as recently reviewed [53]. In malignant cells with adequate nutrient conditions, CIP2A+ cells may outcompete normal cells for nutrients, as AMPK-driven catabolic processes are likely increased, involving glucose uptake and enhanced ATP production by OXPHOS, despite lower glycolytic activity. Conversely, in a low nutrient environment of rapidly growing or necrotic epithelial tumours or in the hypoxia of the marrow niche, cells with high CIP2A levels may have AMPK activity suppressed to lower levels than if well supplied with nutrients, which may relieve AMPK inhibition of mTOR signalling, driving anabolic processes such as protein synthesis and cell growth, whose dysregulation is known to contribute to malignancy and other cellular dysfunction [54]. Similar observations have been shown in human breast cancer cells, where elevated CIP2A led to enhanced mTORC1 activity [55]. In a high nutrient environment with high CIP2A

levels, both catabolic and anabolic processes can therefore occur at the same time, directed by both AMPK and mTORC1, as recently reviewed in CML [53].

In summary, a novel action of CIP2A on energy metabolism is described. Further work is needed to investigate how CIP2A affects AMPK activity and how this is modified by the prevailing nutrient availability, since targeting this interaction may be a potential Achilles heel of the malignant cell.

ACKNOWLEDGEMENTS

The authors gratefully acknowledge the advice and contributions of Drs. Amy Chadwick and Gina Eagle.

DECLARATIONS of INTEREST

All authors have no competing interests to declare.

AUTHOR CONTRIBUTIONS

JAA designed and carried out the majority of experiments with assistance from GMA, and co-wrote the manuscript. LS, MG and KD constructed the cell lines and CML provided intellectual input. RJ acquired mass spectrometry data and advised on data analysis. REC supervised the project and co-wrote the manuscript. All authors approved the final manuscript.

REFERENCES

1 Cristóbal, I., Rincón, R., Manso, R., Madoz-Gúrpide, J., Caramés, C., del Puerto-Nevado, L., et al. (2014) Hyperphosphorylation of PP2A in colorectal cancer and the potential therapeutic value showed by its forskolin-induced dephosphorylation and activation. Biochim. Biophys. Acta 1842, 1823–1829.

2 Soo Hoo, L., Zhang, J. Y. and Chan, E. K. L. (2002) Cloning and characterization of a novel 90 kDa “companion” auto-antigen of p62 overexpressed in cancer. Oncogene 21, 5006–5015.

3 Junttila, M. R., Puustinen, P., Niemelä, M., Ahola, R., Arnold, H., Böttzauw, T., et al. (2007) CIP2A Inhibits PP2A in Human Malignancies. Cell 130, 51–62.

4 Tang M, Shen JF, Li P, Zhou LN, Zeng P, Cui XX., et al. (2018) Prognostic significance of CIP2A expression in solid tumors: A meta-analysis.PLoS ONE 13, e0199675.

5 Lucas, C. M., Harris, R. J., Giannoudis, A., Copland, M., Slupsky, J. R. and Clark, R. E. (2011) Cancerous inhibitor of PP2A (CIP2A) at diagnosis of chronic myeloid leukemia is a critical determinant of disease progression. Blood 117, 6660–6668.

6 Lucas, C. M., Harris, R. J., Holcroft, A. K., Scott, L. J., Carmell, N., McDonald, E., et al. (2015) Second generation tyrosine kinase inhibitors prevent disease progression in high-risk (high CIP2A) chronic myeloid leukaemia patients. Leukemia 29, 1514–1523.

7 Lucas, C. M., Scott, L. J., Carmell, N., Holcroft, A. K., Hills, R. K., Burnett, A. K., et al. (2018) CIP2A- and SETBP1-mediated PP2A inhibition reveals AKT S473 phosphorylation to be a new biomarker in AML. Blood Adv. 2, 964–968.

8 Wang, J., Okkeri, J., Pavic, K., Wang, Z., Kauko, O., Halonen, T., et al. (2017) Oncoprotein CIP2A is stabilized via interaction with tumor suppressor PP2A/B56. EMBO Rep. 18, 437–450.

9 Kerosuo, L., Fox, H., Perälä, N., Ahlqvist, K., Suomalainen, A., Westermarck, J., et al. (2010) CIP2A increases self-renewal and is linked to Myc in neural progenitor cells. Differ. Res. Biol. Divers. 80, 68–77.

10 Niemelä, M., Kauko, O., Sihto, H., Mpindi, J.-P., Nicorici, D., Pernilä, P., et al. (2012) CIP2A signature reveals the MYC dependency of CIP2A-regulated phenotypes and its clinical association with breast cancer subtypes. Oncogene 31, 4266–4278.

11 Myant, K., Qiao, X., Halonen, T., Come, C., Laine, A., Janghorban, M., et al. (2015) Serine 62-Phosphorylated MYC Associates with Nuclear Lamins and Its Regulation by CIP2A Is Essential for Regenerative Proliferation. Cell Rep. 12, 1019–1031.

12 Bagnall, J., Boddington, C., Boyd, J., Brignall, R., Rowe, W., Jones, N. A., et al. (2015) Quantitative dynamic imaging of immune cell signalling using lentiviral gene transfer. Integr. Biol. Quant. Biosci. Nano Macro 7, 713–725.

13 Reed, S. E., Staley, E. M., Mayginnes, J. P., Pintel, D. J. and Tullis, G. E. (2006) Transfection of mammalian cells using linear polyethylenimine is a simple and effective means of producing recombinant adeno-associated virus vectors. J. Virol. Methods 138, 85–98.

14 Peterson, G. L. (1979) Review of the Folin phenol protein quantitation method of Lowry, Rosebrough, Farr and Randall. Anal. Biochem. 100, 201–220.

15 Eagle, G. L., Zhuang, J., Jenkins, R. E., Till, K. J., Jithesh, P. V., Lin, K., et al. (2015) Total Proteome Analysis Identifies Migration Defects as a Major Pathogenetic Factor in Immunoglobulin Heavy Chain Variable Region (IGHV)-unmutated Chronic Lymphocytic Leukemia. Mol. Cell. Proteomics MCP 14, 933–945.

16 Tyanova, S., Temu, T., Sinitcyn, P., Carlson, A., Hein, M. Y., Geiger, T., et al. (2016) The Perseus computational platform for comprehensive analysis of (prote)omics data. Nat. Methods 13, 731–740.

17 Huang, D. W., Sherman, B. T. and Lempicki, R. A. (2009) Bioinformatics enrichment tools: paths toward the comprehensive functional analysis of large gene lists. Nucleic Acids Res. 37, 1–13.

18 Huang, D. W., Sherman, B. T. and Lempicki, R. A. (2009) Systematic and integrative analysis of large gene lists using DAVID bioinformatics resources. Nat. Protoc. 4, 44–57.

19 Shannon, P., Markiel, A., Ozier, O., Baliga, N. S., Wang, J. T., Ramage, D., et al. (2003) Cytoscape: a software environment for integrated models of biomolecular interaction networks. Genome Res. 13, 2498–2504.

20 Smoot, M. E., Ono, K., Ruscheinski, J., Wang, P.-L. and Ideker, T. (2011) Cytoscape 2.8: new features for data integration and network visualization. Bioinforma. Oxf. Engl. 27, 431–432.

21 Szklarczyk, D., Morris, J. H., Cook, H., Kuhn, M., Wyder, S., Simonovic, M., et al. (2017) The STRING database in 2017: quality-controlled protein–protein association networks, made broadly accessible. Nucleic Acids Res. 45, D362–D368.

22 Pallai, R., Bhaskar, A., Barnett-Bernodat, N., Gallo-Ebert, C., Pusey, M., Nickels, J. et al. (2015) Leucine-rich repeat-containing protein 59 mediates nuclear import of cancerous inhibitor of PP2A in prostate cancer cells. Tumor Biol. 8, 6683-6390.

23 Cha, G., Xu, J., Xu, X., Li, B., Lu, S., Nanding, A., et al. (2017) High expression of CIP2A protein is associated with tumor aggressiveness in stage I–III NSCLC and correlates with poor prognosis. OncoTargets Ther. 10, 5907-5914.

24 Kanehisa, M., Goto, S., Kawashima, S., Okuno, Y. and Hattori, M. (2004) The KEGG resource for deciphering the genome. Nucleic Acids Res. 32, D277-280.

25 Stein, S. C., Woods, A., Jones, N. A., Davison, M. D. and Carling, D. (2000) The regulation of AMP-activated protein kinase by phosphorylation. Biochem. J. 345 Pt 3, 437–443.

26 Jäger S, Handschin C, St.-Pierre J, Spiegelman BM. (2007) AMP-activated protein kinase (AMPK) action in skeletal muscle via direct phosphorylation of PGC-1α. Proc. Natl. Acad. Sci. U. S. A. 104, 12017–12022.

27 Herzig S and Shaw RJ. (2018) AMPK: guardian of metabolism and mitochondrial homeostasis. Nat Rev Mol Cell Biol. 19, 121–135.

28 Xi G, Rosen CJ and Clemmons DR. (2016) IGF-I and IGFBP-2 stimulate AMPK activation and autophagy, which are required for osteoblast differentiation. Endocrinology. 157, 268–281.

29 Tanida I, Ueno T, Kominami E. (2008) LC3 and autophagy. Methods Mol. Biol. Clifton NJ. 445, 77–88.

30 Kadowaki M, Karim MR. (2009) Cytosolic LC3 ratio as a quantitative index of macroautophagy. Methods Enzymol. 452, 199-213.

31 Santidrián , A. F., González-Gironès, D. M., Iglesias-Serret, D., Coll-Mulet, L., Cosialls, A. M., Frias, M. de, Campàs, C., et al. (2010) AICAR induces apoptosis independently of AMPK and p53 through up-regulation of the BH3-only proteins BIM and NOXA in chronic lymphocytic leukemia cells. Blood 116, 3023–3032.

32 Kwon, H. J., Rhim, J. H., Jang, I.-S., Kim, G.-E., Park, S. C. and Yeo, E.-J. (2010) Activation of AMP-activated protein kinase stimulates the nuclear localization of glyceraldehyde 3-phosphate dehydrogenase in human diploid fibroblasts. Exp. Mol. Med. 42, 254–269.

33 Liberti, M. V. and Locasale, J. W. (2016) The Warburg Effect: How Does it Benefit Cancer Cells? Trends Biochem. Sci. 41, 211–218.

34 Estrella, V., Chen, T., Lloyd, M., Wojtkowiak, J., Cornnell, H. H., Ibrahim-Hashim, A., et al. (2013) Acidity generated by the tumor microenvironment drives local invasion. Cancer Res. 73, 1524–1535.

35 Jeong, A. L., Ka, H. I., Han, S., Lee, S., Lee, E.-W., Soh, S. J., et al. (2018) Oncoprotein CIP2A promotes the disassembly of primary cilia and inhibits glycolytic metabolism. EMBO Rep. 19. E45144.

36 Peng, B., Lei, N., Chai, Y., Chan, E. K. L. and Zhang, J.-Y. (2015) CIP2A regulates cancer metabolism and CREB phosphorylation in non-small cell lung cancer. Mol. Biosyst. 11, 105–114.

37 Crabtree, H. G. (1929) Observations on the carbohydrate metabolism of tumours. Biochem. J. 23, 536–545.

38 Cheung, P. C., Salt, I. P., Davies, S. P., Hardie, D. G. and Carling, D. (2000) Characterization of AMP-activated protein kinase gamma-subunit isoforms and their role in AMP binding. Biochem. J. 346 Pt 3, 659–669.

39 Mihaylova, M. M. and Shaw, R. J. (2011) The AMP-activated protein kinase (AMPK) signaling pathway coordinates cell growth, autophagy, & metabolism. Nat. Cell Biol. 13, 1016–1023.

40 Wu, S.-B. and Wei, Y.-H. (2012) AMPK-mediated increase of glycolysis as an adaptive response to oxidative stress in human cells: Implication of the cell survival in mitochondrial diseases. Biochim. Biophys. Acta BBA - Mol. Basis Dis. 1822, 233–247.

41 Marin, T. L., Gongol, B., Zhang, F., Martin, M., Johnson, D. A., Xiao, H., et al. (2017) AMPK promotes mitochondrial biogenesis and function by phosphorylating the epigenetic factors DNMT1, RBBP7, and HAT1. Sci. Signal. 10. eaaf7478.

42 Zhao, B., Qiang, L., Joseph, J., Kalyanaraman, B., Viollet, B. and He, Y.-Y. (2016) Mitochondrial dysfunction activates the AMPK signaling and autophagy to promote cell survival. Genes Dis. 3, 82–87.

43 Kishton, R. J., Barnes, C. E., Nichols, A. G., Cohen, S., Gerriets, V. A., Siska, P. J., et al. (2016) AMPK is essential to balance glycolysis and mitochondrial metabolism to control T-ALL cell stress and survival. Cell Metab. 23, 649–662.

44 Joseph, B. K., Liu, H.-Y., Francisco, J., Pandya, D., Donigan, M., Gallo-Ebert, C., et al. (2015) Inhibition of AMP Kinase by the Protein Phosphatase 2A Heterotrimer, PP2APpp2r2d. J. Biol. Chem. 290, 10588–10598.

45 Coughlan, K. A., Balon, T. W., Valentine, R. J., Petrocelli, R., Schultz, V., Brandon, A., et al. (2015) Nutrient Excess and AMPK Downregulation in Incubated Skeletal Muscle and Muscle of Glucose Infused Rats. PloS One 10, e0127388.

46 Kim, K. -y., Baek, A., Hwang, J.-E., Choi, Y. A., Jeong, J., Lee, M.-S., et al. (2009) Adiponectin-Activated AMPK Stimulates Dephosphorylation of AKT through Protein Phosphatase 2A Activation. Cancer Res. 69, 4018–4026.

47 Cantó, C. and Auwerx, J. (2010) AMP-activated protein kinase and its downstream transcriptional pathways. Cell. Mol. Life Sci. CMLS 67, 3407–3423.

48 Thomson, D. M., Herway, S. T., Fillmore, N., Kim, H., Brown, J. D., Barrow, J. R. et al. (2008) AMP-activated protein kinase phosphorylates transcription factors of the CREB family. J. Appl. Physiol. Bethesda Md 1985 104, 429–438.

49 Weikel, K. A., Cacicedo, J. M., Ruderman, N. B. and Ido, Y. Glucose and palmitate uncouple AMPK from autophagy in human aortic endothelial cells. Am. J. Physiol. Cell Physiol. 2015; 308, C249-263 .

50 Dalle Pezze, P., Ruf, S., Sonntag, A. G., Langelaar-Makkinje, M., Hall, P., Heberle, A.M. et al. (2016) A systems study reveals concurrent activation of AMPK and mTOR by amino acids. Nat.Comm. 7, 13254

51 Kuntz, E. M., Baquero, P., Michie, A. M., Dunn, K., Tardito, S., Holyoake, T. L., et al. (2017) Targeting mitochondrial oxidative phosphorylation eradicates therapy-resistant chronic myeloid leukemia stem cells. Nat. Med. 23, 1234–1240.

52 Mitchell, R., Hopcroft, L. E. M., Baquero, P., Allan, E. K., Hewit, K., James, D., et al. (2017) Targeting BCR-ABL-Independent TKI Resistance in Chronic Myeloid Leukemia by mTOR and Autophagy Inhibition. JNCI J. Natl. Cancer Inst. 110, 467–478.

53 Baquero, P., Dawson, A. and Helgason, G. V. (2018) Autophagy and Mitochondrial Metabolism: Insights into their Role and Therapeutic Potential in Chronic Myeloid Leukaemia. FEBS J. [Epub ahead of print]

54 Zoncu, R., Efeyan, A. and Sabatini, D. M. (2011) mTOR: from growth signal integration to cancer, diabetes and ageing. Nat. Rev. Mol. Cell Biol. 12, 21–35.

55 Puustinen, P., Rytter, A., Mortensen, M., Kohonen, P., Moreira, J. M. and Jäättelä, M. (2014) CIP2A oncoprotein controls cell growth and autophagy through mTORC1 activation. J Cell Biol 204, 713–727.

Figure 1. Validation of CIP2A status in lentiviral K562 cell lines and fractionation.
Panel A: Western blot analysis and resultant densitometry plots demonstrating the relative level of CIP2A and functionally associated proteins MYC and PP2A between unmodified and CIP2A modified cell lines. Levels are expressed as mean +/- standard error of at least 3 replicates. * denotes $p < 0.05$ using unpaired Student's T –test). Panel B: Cytoplasmic and nuclear fractionation of unmodified and CIP2A modified cell lysates showing cellular location of CIP2A, MYC and P-Tyr-307-PP2A and PP2A's catalytic subunit. Panel C: Distribution of cell population in flow cytometry side and forward scatter, with relative sizes demonstrated through forward scatter overlay in high (24h after feeding) and low (72h after feeding) nutrient conditions. Panel D: Effect of starvation on viability in CIP2A modified cells after 72h media starvation, determined through annexin V and propidium iodide (PI) uptake in flow cytometry.

Figure 2. The effect of CIP2A level on seahorse energy metabolic stress assays of glycolysis (panels A-E) and OXPHOS (panels F-K).
Panel A: Annotated experimental data for the CIP2A manipulated and unmodified cell lines, normalised to the non-glycolytic acidification (mean of 3 experiments with standard errors). Compounds were injected at times indicated to manipulate glycolysis and measure different metabolic components through changes in the levels of extracellular acidification rate (ECAR). Panel B, basal glycolysis (** $p<0.0001$), Panel C, maximum glycolytic capacity and Panel D, spare capacity (* $p=0.0435$, ** $p<0.002$) express these data as means +/- standard error from their 3 contributory time points (each with n=3). Statistical analysis is by unpaired Student's T-test, with Welch correction).
Panel E: Experimental profiles for OXPHOS, annotated with compounds injected and components of OXPHOS that were measured through assessing levels of the oxygen consumption rate (OCR). Panels F-I depict the data of panel E analogous to that of panels A and B-D; (mean of 3 experiments with standard error). Panel F, basal aerobic respiration (* $p=0.0353$, ** $p<0.0001$), Panel G, ATP production (** <0.0001), Panel H, maximum respiration (** $p<0.005$) and Panel I, spare mitochondrial capacity (** $p<0.007$). Time points used as indicated by * in panel A and E respectively

Figure 3. CIP2A driven proteomic changes assessed by quantitative mass spectrometry and ITRAQ.
Panel A: Heat map showing 229 proteins whose expression in either (or both) CIP2A+ or CIP2A- differed significantly (FE $p < 0.05$; see text) from unmodified cells. Panel B: Heat map of DAVID analysis on upregulated proteins and enrichment in energy metabolic pathways as identified by KEGG (FE $p <0.05$). Panel C: DAVID analysis on proteins down regulated with elevated CIP2A and KEGG pathway enrichment in energy metabolic processes (FE $p<0.05$).

Figure 4. CIP2A associating proteins. Panel A; Venn diagram showing the total proteins derived from the N- and C-terminus targeted immunoprecipitation experiments (IP#1 and IP#2) and CIP2A-venus extraction. Panel B: These 52 common proteins were input into the functional protein interaction network STRING software. Proteins are represented by circular

nodes and interactions by a straight line edge, with line thickness representing the confidence of the interaction based on experimental, co-expression and text mining data incorporated within STRING search parameters (17). Interaction confidence limit was set to medium (0.4 out of 1.0). Proteins enriched using DAVID are shown as coloured nodes alongside the identified KEGG pathway and enrichment p value.

Figure 5. CIP2A nutrient dependent regulation of AMPK. Panel A: Western blot showing levels of CIP2A, AMPK, P-Thr-172 AMPK , P-Ser-62-Myc, the AMPK substrate GLUT4 and actin loading controls in low (fed 72 hours earlier) and high (fed 24 hours earlier) nutrient conditions, with relative quantitation by densitometry, normalised to the low unmodified condition (n=3, unpaired Student T-test) * and ** indicate $p<0.05$ and <0.01 respectively. Panel B: Western blots of ULK-1 phosphorylation at Ser555 (P-Ser-555-ULK-1) and LC3I and II, markers of autophagy, in low (72h) and high (24h) nutrient states, with relative quantitation of the LC3II/LC3I ratio. * and ** are as for panel A. Panel C: PP2A inhibition by the phosphatase inhibitor okadaic acid at 5 and 10 nMolar in CIP2A- cells, showing an increase in AMPK activity (P-Thr-172-AMPK).

Figure 6. Manipulation of AMPK activity can regulate OXPHOS activity.
Panel A: OXPHOS assay in CIP2A- cells in high nutrient conditions (i.e. low AMPK activity), with AICAR added as shown, and effect on P-Ser-172-AMPK level as shown by western blot. Panel B: Column plots for the experiment in panel A: * = $p<0.05$, ** = $p<0.01$. Panel C: OXPHOS assay in CIP2A+ cells in high nutrient conditions (i.e. high AMPK activity) showing the effect of Compound C (CC) on basal and maximal OXPHOS capacity and effect on P-Ser-172-AMPK level. Panel D: column plots of the experiment in panel D. * = $p<0.05$ and ** = $p<0.01$.

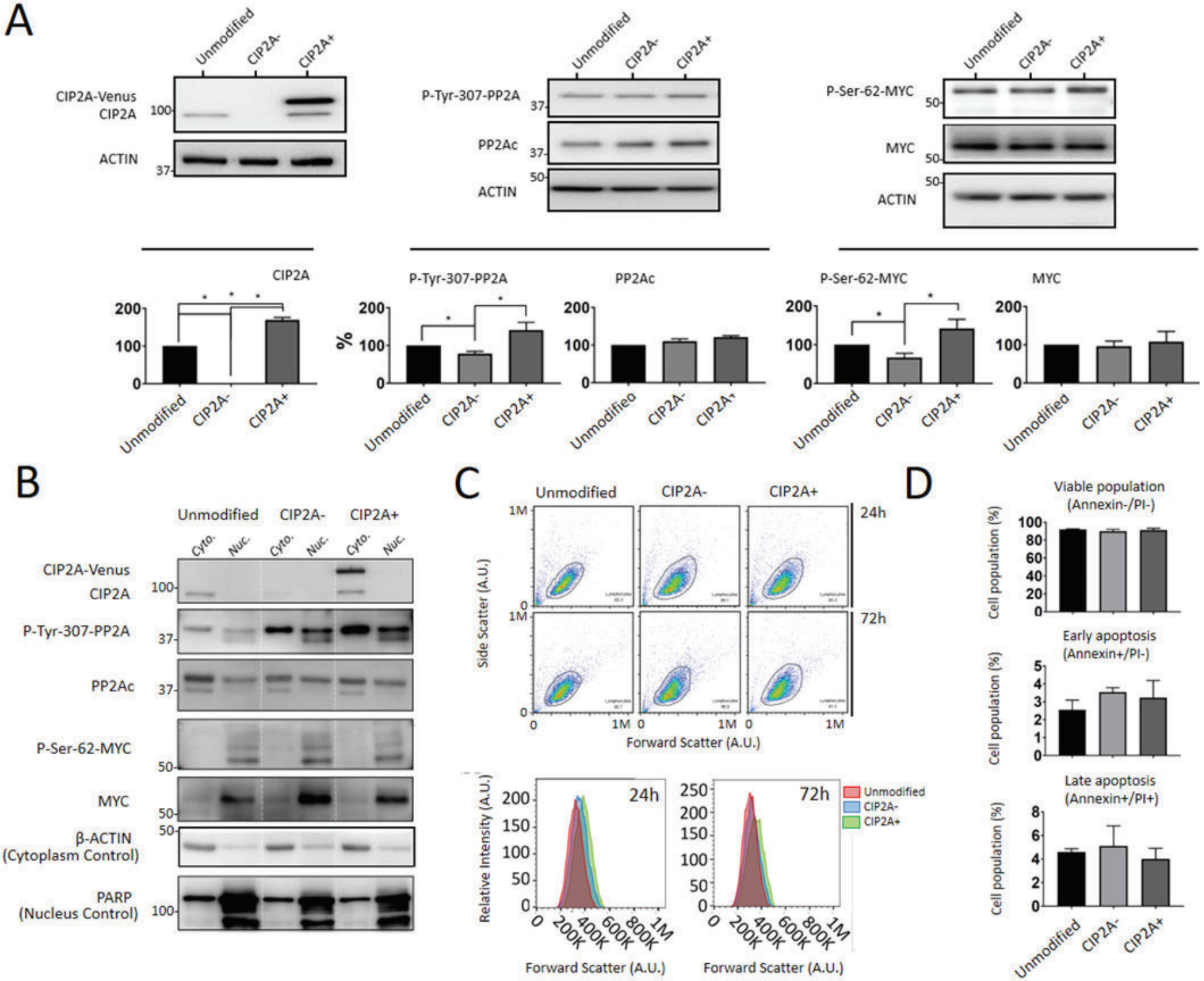
A
Unmodified
CIP2A-
CIP2A+
CIP2A-Venus
CIP2A
ACTIN
P-Tyr-307-PP2A
PP2Ac
P-Ser-62-MYC
MYC
CIP2A
P-Tyr-307-PP2A
PP2Ac
P-Ser-62-MYC
MYC
B
Cyto.
Nuc.
β-ACTIN
(Cytoplasm Control)
PARP
(Nucleus Control)
C
Side Scatter (A.U.)
Forward Scatter (A.U.)
24h
72h
Relative Intensity (A.U.)
D
Viable population
(Annexin-/PI-)
Early apoptosis
(Annexin+/PI-)
Late apoptosis
(Annexin+/PI+)
Cell population (%)

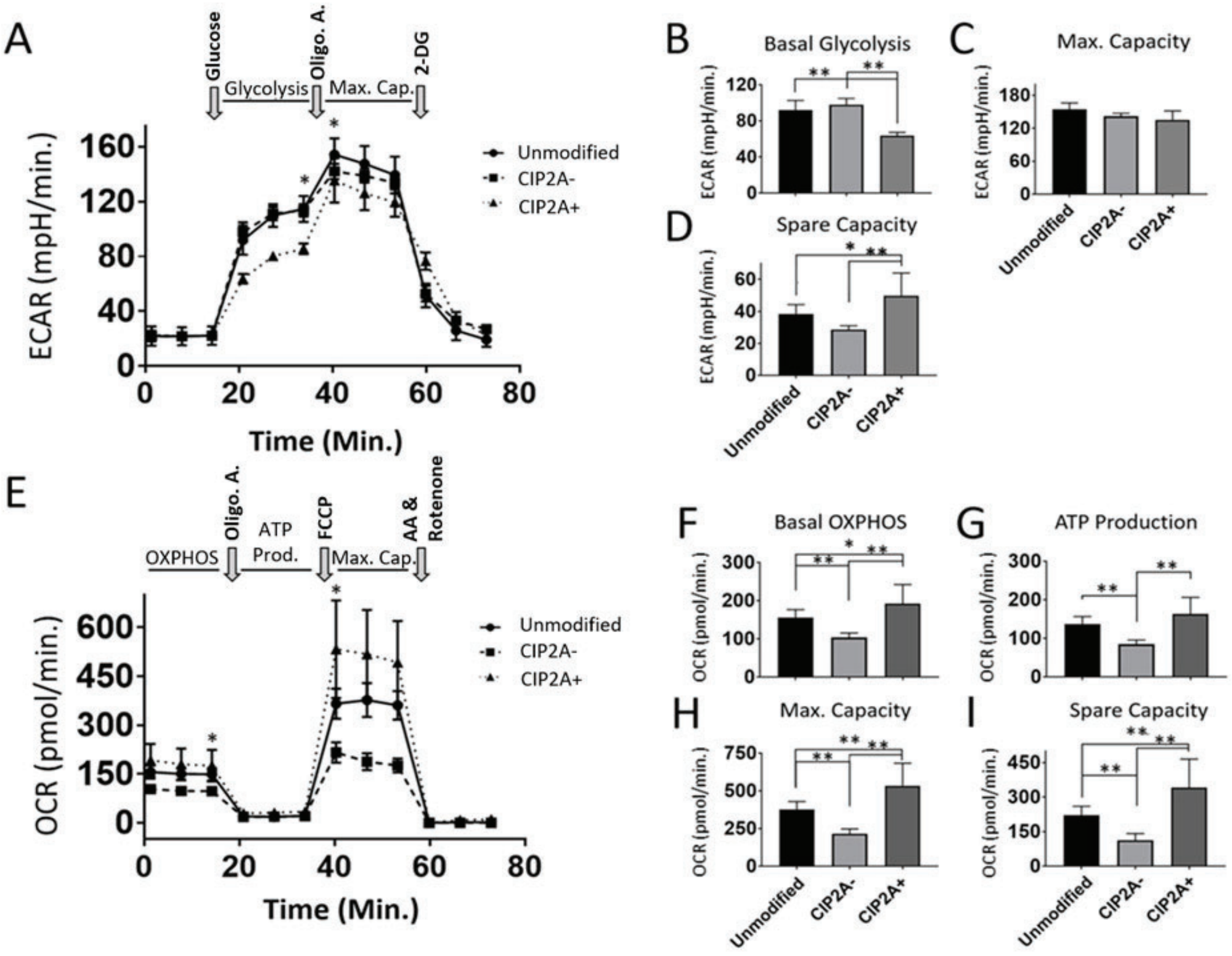
A
Glucose
Oligo. A.
2-DG
Glycolysis
Max. Cap.
ECAR (mpH/min.)
Time (Min.)
Unmodified
CIP2A-
CIP2A+
B
Basal Glycolysis
C
Max. Capacity
D
Spare Capacity
E
Oligo. A.
FCCP
AA & Rotenone
OXPHOS
ATP Prod.
Max. Cap.
OCR (pmol/min.)
F
Basal OXPHOS
G
ATP Production
H
Max. Capacity
I
Spare Capacity

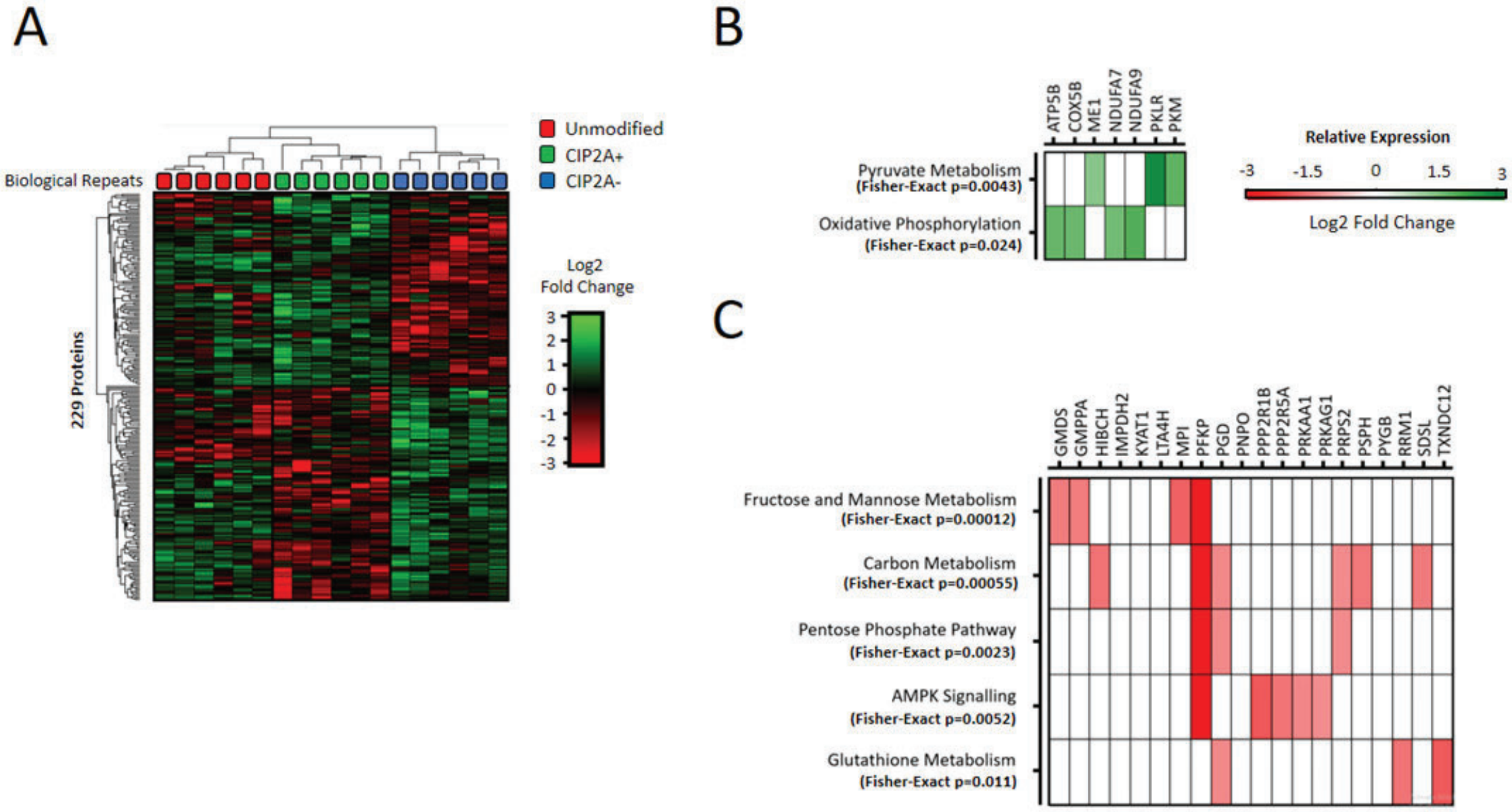
A
Biological Repeats
229 Proteins
Unmodified
CIP2A+
CIP2A-
Log2
Fold Change
3
2
1
0
-1
-2
-3
B
ATP5B
COX5B
ME1
NDUFA7
NDUFA9
PKLR
PKM
Pyruvate Metabolism
(Fisher-Exact p=0.0043)
Oxidative Phosphorylation
(Fisher-Exact p=0.024)
Relative Expression
-3
-1.5
0
1.5
3
Log2 Fold Change
C
GMDS
GMPPA
HIBCH
IMPDH2
KYAT1
LTA4H
MPI
PFKP
PGD
PNPO
PPP2R1B
PPP2R5A
PRKAA1
PRKAG1
PRPS2
PSPH
PYGB
RRM1
SDSL
TXNDC12
Fructose and Mannose Metabolism
(Fisher-Exact p=0.00012)
Carbon Metabolism
(Fisher-Exact p=0.00055)
Pentose Phosphate Pathway
(Fisher-Exact p=0.0023)
AMPK Signalling
(Fisher-Exact p=0.0052)
Glutathione Metabolism
(Fisher-Exact p=0.011)

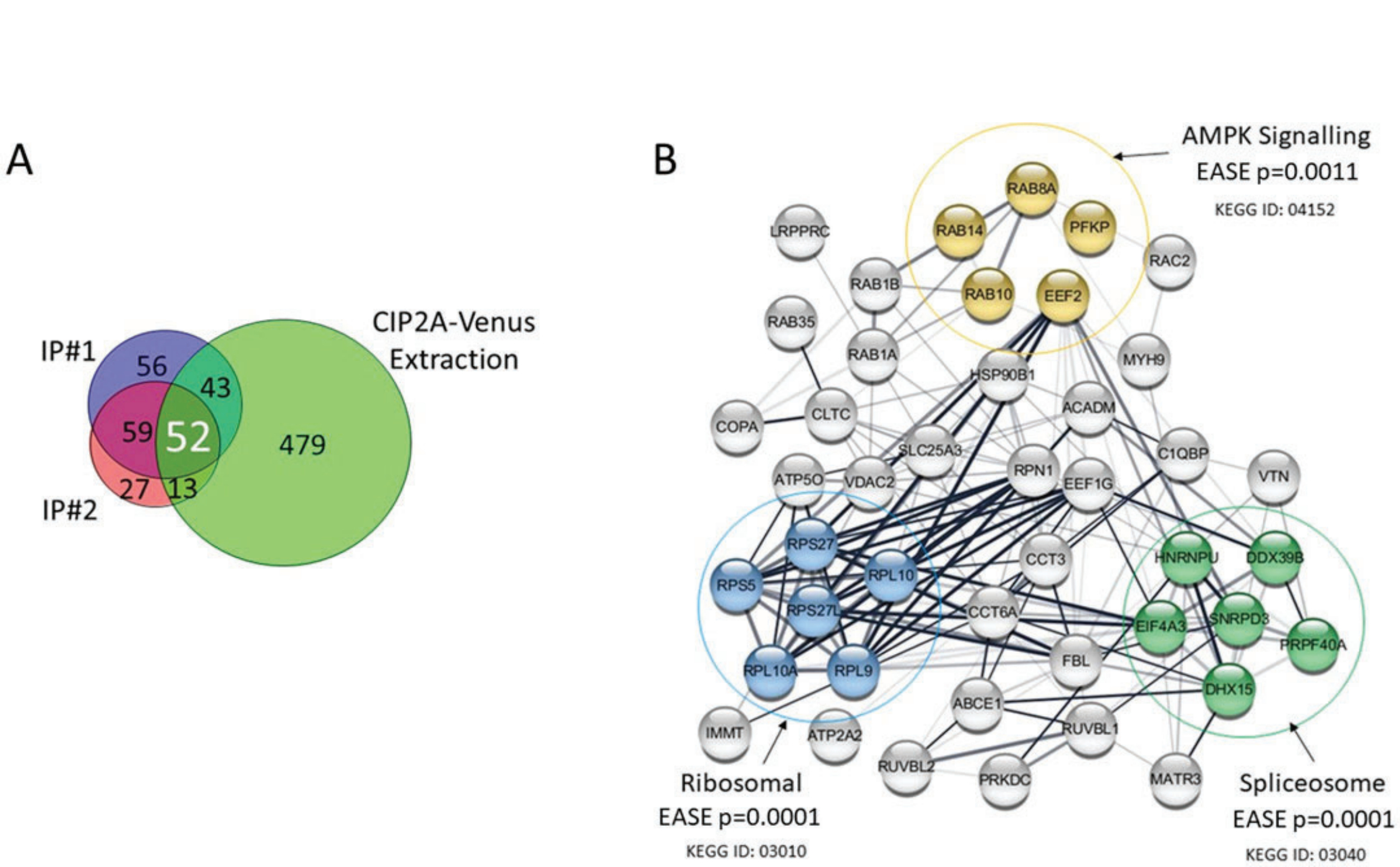
A
IP#1
56
43
59
52
479
27
13
IP#2
CIP2A-Venus
Extraction
B
AMPK Signalling
EASE p=0.0011
KEGG ID: 04152
RAB8A
RAB14
PFKP
LRPPRC
RAC2
RAB1B
RAB10
EEF2
RAB35
RAB1A
MYH9
HSP90B1
ACADM
COPA
CLTC
SLC25A3
C1QBP
RPN1
EEF1G
VTN
ATP5O
VDAC2
RPS27
CCT3
HNRNPU
DDX39B
RPS5
RPL10
RPS27L
CCT6A
EIF4A3
SNRPD3
PRPF40A
FBL
RPL10A
RPL9
DHX15
ABCE1
IMMT
ATP2A2
RUVBL1
RUVBL2
PRKDC
MATR3
Ribosomal
EASE p=0.0001
KEGG ID: 03010
Spliceosome
EASE p=0.0001
KEGG ID: 03040

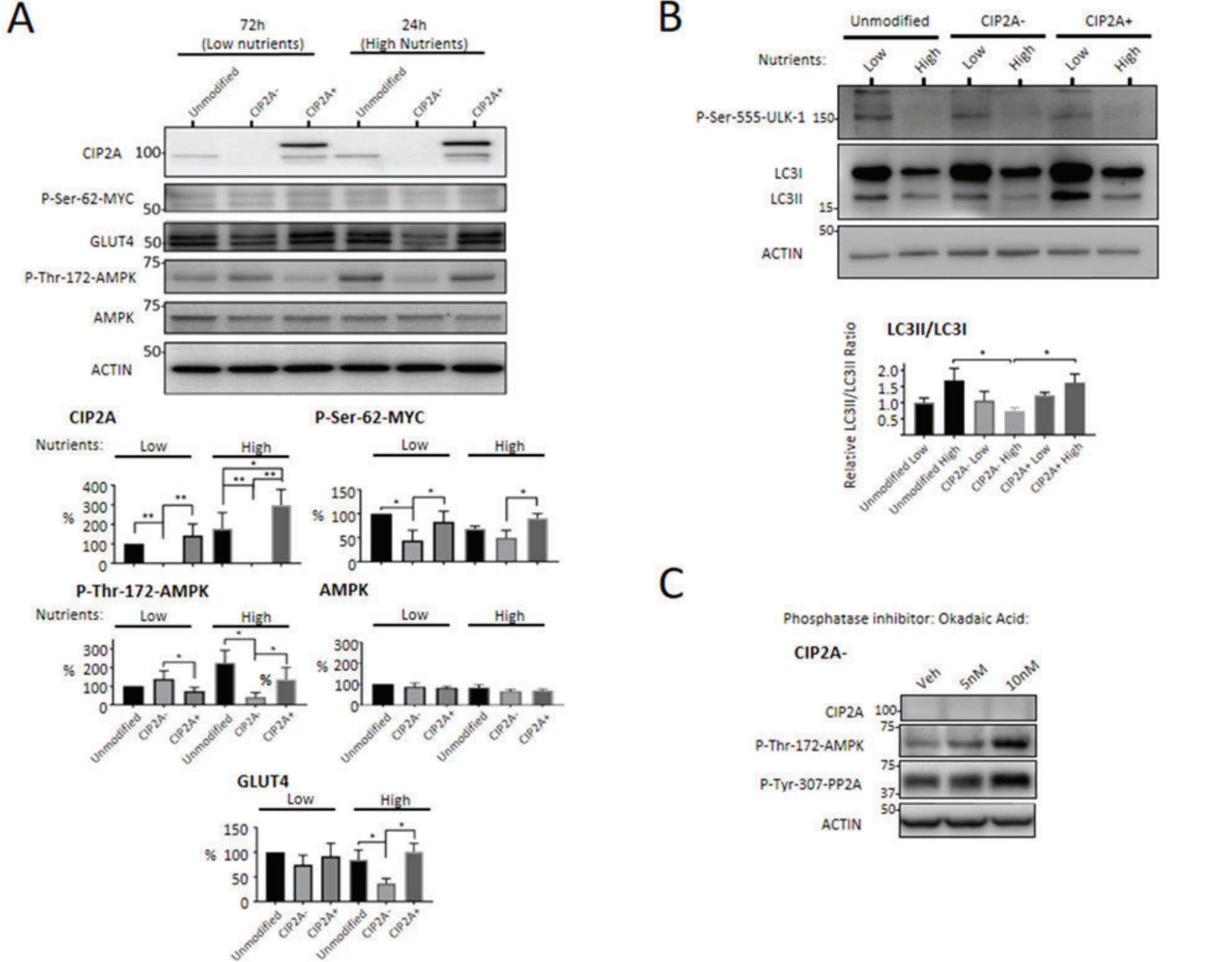
A
72h
(Low nutrients)
24h
(High Nutrients)
Unmodified
CIP2A-
CIP2A+
CIP2A
P-Ser-62-MYC
GLUT4
P-Thr-172-AMPK
AMPK
ACTIN
Nutrients:
Low
High
%
B
Unmodified
CIP2A-
CIP2A+
P-Ser-555-ULK-1
LC3I
LC3II
ACTIN
LC3II/LC3I
Relative LC3II/LC3II Ratio
Unmodified Low
Unmodified High
CIP2A- Low
CIP2A- High
CIP2A+ Low
CIP2A+ High
C
Phosphatase inhibitor: Okadaic Acid:
CIP2A-
Veh
5nM
10nM
P-Tyr-307-PP2A

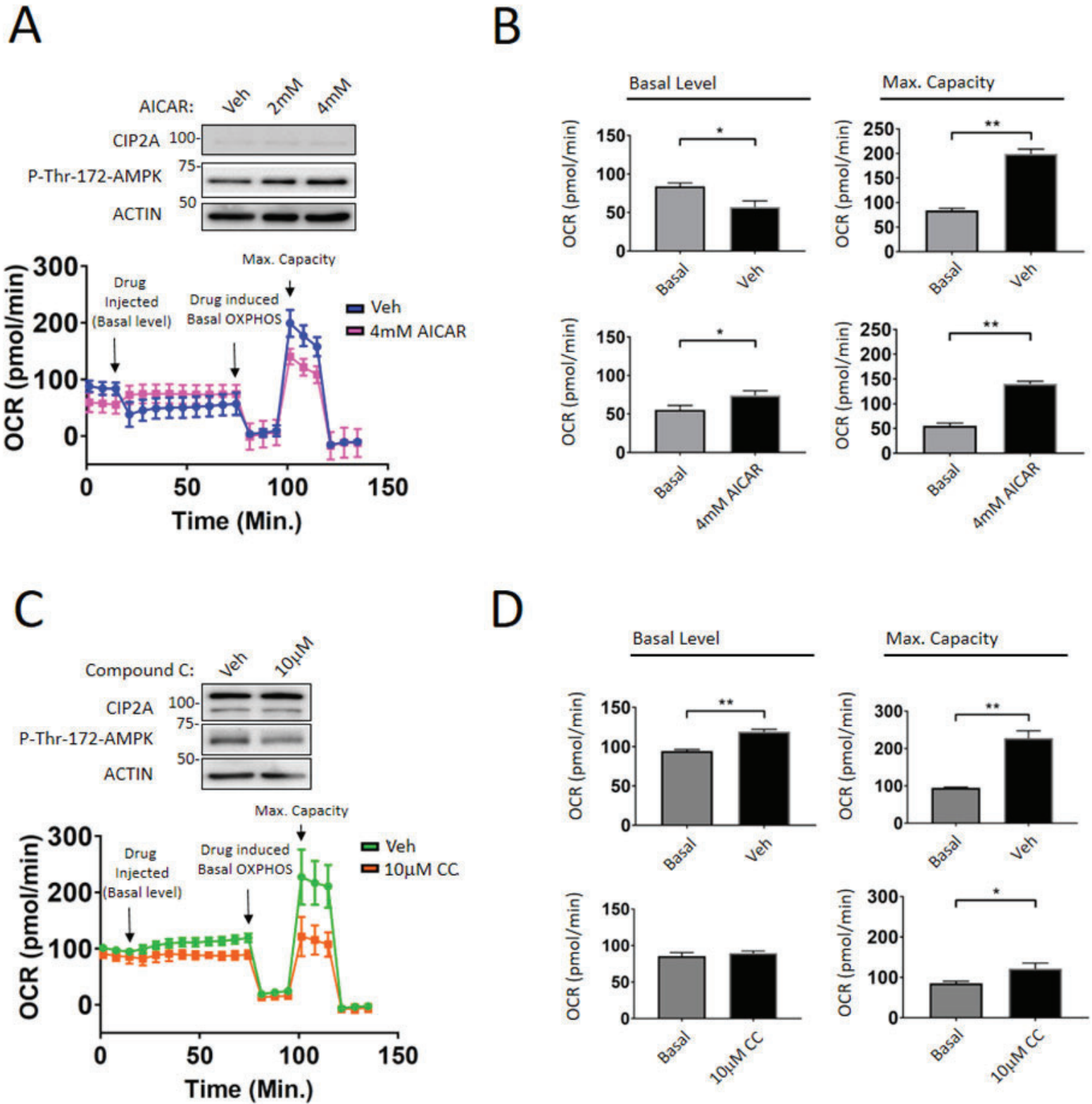
A
AICAR: Veh 2mM 4mM
CIP2A 100-
P-Thr-172-AMPK 75-
ACTIN 50
Max. Capacity
Drug Injected (Basal level)
Drug induced Basal OXPHOS
Veh
4mM AICAR
OCR (pmol/min)
Time (Min.)
B
Basal Level
Max. Capacity
OCR (pmol/min)
Basal
Veh
4mM AICAR
C
Compound C: Veh 10μM
CIP2A 100-
P-Thr-172-AMPK 75-
ACTIN 50
Max. Capacity
Drug Injected (Basal level)
Drug induced Basal OXPHOS
Veh
10μM CC
OCR (pmol/min)
Time (Min.)
D
Basal Level
Max. Capacity
OCR (pmol/min)
Basal
Veh
10μM CC

Supplementary Table S1. Supplementary to Figure 3, list of the 229 proteins that significantly differ between CIP2A+ and CIP2A- cell lines with corresponding Log2 values. Expression calculated on CIP2A+ vs CIP2A- cells ($p < 0.05$, ANOVA, FC = Fold Change). *See supplementary material file.*

Supplementary Table S1.

#	Accession#	Gene ID	Protein Name	Ratio	Log2 FC	pValue
1	Q16698	DECR1	2,4-dienoyl-CoA reductase 1, mitochondrial	0.8	-1.3	0.00750
2	Q6NVY1	HIBCH	3-hydroxyisobutyryl-CoA hydrolase	0.6	-1.6	0.00327
3	P31939	ATIC	5-aminoimidazole-4-carboxamide ribonucleotide formyltransferase/IMP cyclohydrolase	0.7	-1.4	0.00805
4	Q5TFE4	NT5DC1	5'-nucleotidase domain containing 1	0.7	-1.4	0.01309
5	O96019	ACTL6A	actin like 6A	0.7	-1.4	0.01869
6	O43707	ACTN4	actinin alpha 4	0.6	-1.6	0.02803
7	O00154	ACOT7	acyl-CoA thioesterase 7	1.2	1.2	0.00964
8	P55263	ADK	adenosine kinase	0.6	-1.8	0.00776
9	P18085	ARF4	ADP ribosylation factor 4	0.7	-1.5	0.01545
10	P55196	AFDN	afadin, adherens junction formation factor	1.8	1.8	0.00002
11	Q5JTZ9	AARS2	alanyl-tRNA synthetase 2, mitochondrial	0.7	-1.3	0.02558
12	P30038	ALDH4A1	aldehyde dehydrogenase 4 family member A1	0.6	-1.6	0.02827
13	Q13155	AIMP2	aminoacyl tRNA synthetase complex interacting multifunctional protein 2	0.7	-1.4	0.00656
14	Q8IWZ3	ANKHD1	ankyrin repeat and KH domain containing 1	1.4	1.4	0.02536
15	P07355	ANXA2	annexin A2	0.6	-1.6	0.00547
16	P27695	APEX1	apurinic/apyrimidinic endodeoxyribonuclease 1	1.5	1.5	0.02598
17	O43681	bacterial	arsA arsenite transporter, ATP-binding, homolog 1	2.0	2.0	0.00049
18	O43776	NARS	asparaginyl-tRNA synthetase	1.6	1.6	0.00464
19	P06576	ATP5B	ATP synthase, H+ transporting, mitochondrial F1 complex, beta polypeptide	1.6	1.6	0.01267
20	Q5T9A4	ATAD3B	ATPase family, AAA domain containing 3B	1.4	1.4	0.02727
21	Q96GS4	BORCS6	BLOC-1 related complex subunit 6	1.4	1.4	0.01662
22	Q13895	BYSL	bystin like	1.6	1.6	0.00534
23	P0DP25	CALM1	calmodulin 1	0.6	-1.6	0.03004
24	P47756	CAPZB	capping actin protein of muscle Z-line beta subunit	0.7	-1.5	0.01821
25	P27708	CAD	carbamoyl-phosphate synthetase 2, aspartate transcarbamylase, and dihydroorotase	0.7	-1.5	0.02329
26	P42574	CASP3	caspase 3	0.8	-1.3	0.02782
27	P35221	CTNNA1	catenin alpha 1	1.6	1.6	0.00187
28	Q8IX12	CCAR1	cell division cycle and apoptosis regulator 1	0.6	-1.6	0.00331
29	P49454	CENPF	centromere protein F	0.6	-1.6	0.00688
30	P78371	CCT2	chaperonin containing TCP1	0.7	-1.4	0.00812

			subunit 2			
31	P50991	CCT4	chaperonin containing TCP1 subunit 4	0.7	-1.4	0.02356
32	P48643	CCT5	chaperonin containing TCP1 subunit 5	0.6	-1.6	0.02345
33	P40227	CCT6A	chaperonin containing TCP1 subunit 6A	0.6	-1.6	0.00229
34	Q99832	CCT7	chaperonin containing TCP1 subunit 7	0.6	-1.6	0.00301
35	Q9H444	CHMP4B	charged multivesicular body protein 4B	1.5	1.5	0.00727
36	Q86X55	CARM1	coactivator associated arginine methyltransferase 1	1.4	1.4	0.01308
37	Q9UBF2	COPG2	coatomer protein complex subunit gamma 2	0.6	-1.6	0.01454
38	O60826	CCDC22	coiled-coil domain containing 22	1.2	1.2	0.01807
39	Q13951	CBFB	core-binding factor beta subunit	0.8	-1.3	0.00336
40	Q9BR76	CORO1B	coronin 1B	0.7	-1.4	0.01143
41	Q9NRF8	CTPS2	CTP synthase 2	0.7	-1.3	0.02115
42	Q9P0U4	CXXC1	CXXC finger protein 1	1.2	1.2	0.02611
43	P24941	CDK2	cyclin dependent kinase 2	0.6	-1.7	0.00699
44	P10606	COX5B	cytochrome c oxidase subunit 5B	1.6	1.6	0.01818
45	O76071	CIAO1	cytosolic iron-sulfur assembly component 1	0.8	-1.2	0.02340
46	Q16531	DDB1	damage specific DNA binding protein 1	0.7	-1.4	0.01468
47	Q96GQ7	DDX27	DEAD-box helicase 27	1.2	1.2	0.01984
48	P26196	DDX6	DEAD-box helicase 6	0.7	-1.4	0.00307
49	P35659	DEK	DEK proto-oncogene	0.7	-1.4	0.00927
50	Q7L2E3	DHX30	DExH-box helicase 30	1.4	1.4	0.02009
51	Q68CQ4	zebrafish	digestive organ expansion factor homolog	1.3	1.3	0.01282
52	P00374	DHFR	dihydrofolate reductase	1.3	1.3	0.01682
53	O43314	PPIP5K2	diphosphoinositol pentakisphosphate kinase 2	2.0	2.0	0.00012
54	Q8IYB7	DIS3L2	DIS3 like 3'-5' exoribonuclease 2	0.7	-1.5	0.02074
55	P25685	DNAJB1	DnaJ heat shock protein family (Hsp40) member B1	1.8	1.8	0.00038
56	Q9NVH1	DNAJC11	DnaJ heat shock protein family (Hsp40) member C11	1.5	1.5	0.00969
57	Q99543	DNAJC2	DnaJ heat shock protein family (Hsp40) member C2	0.7	-1.4	0.00117
58	Q9UNI6	DUSP12	dual specificity phosphatase 12	0.7	-1.4	0.01910
59	Q13409	DYNC1I2	dynein cytoplasmic 1 intermediate chain 2	0.7	-1.5	0.00172
60	P63167	DYNLL1	dynein light chain LC8-type 1	0.7	-1.4	0.00194
61	Q96HE7	ERO1A	endoplasmic reticulum oxidoreductase 1 alpha	0.6	-1.6	0.01905
62	O43491	EPB41L2	erythrocyte membrane protein band 4.1 like 2	2.1	2.1	0.01171
63	Q05639	EEF1A2	eukaryotic translation elongation factor 1 alpha 2	0.5	-1.9	0.02423
64	P05198	EIF2S1	eukaryotic translation initiation factor 2 subunit alpha	1.5	1.5	0.00048
65	P20042	EIF2S2	eukaryotic translation initiation factor 2 subunit beta	1.6	1.6	0.00033
66	P41091	EIF2S3	eukaryotic translation initiation factor 2 subunit gamma	1.8	1.8	0.00148
67	Q15056	EIF4H	eukaryotic translation initiation factor 4H	1.7	1.7	0.00728

68	Q8TAG9	EXOC6	exocyst complex component 6	0.7	-1.4	0.00945
69	Q06265	EXOSC9	exosome component 9	1.5	1.5	0.01084
70	Q96TA1	FAM129B	family with sequence similarity 129 member B	0.6	-1.6	0.00030
71	Q9Y3D0	FAM96B	family with sequence similarity 96 member B	0.7	-1.4	0.00703
72	Q96AE4	FUBP1	far upstream element binding protein 1	0.6	-1.6	0.01686
73	P14324	FDPS	farnesyl diphosphate synthase	1.5	1.5	0.01210
74	Q14254	FLOT2	flotillin 2	1.9	1.9	0.02498
75	Q8IY81	FTSJ3	FtsJ homolog 3	1.5	1.5	0.00212
76	Q9BVP2	GNL3	G protein nucleolar 3	1.8	1.8	0.00522
77	Q8TAE8	GADD45GIP1	GADD45G interacting protein 1	0.8	-1.2	0.02997
78	Q9NY12	GAR1	GAR1 ribonucleoprotein	1.5	1.5	0.01006
79	P31150	GDI1	GDP dissociation inhibitor 1	0.7	-1.5	0.01866
80	O60547	GMDS	GDP-mannose 4,6-dehydratase	0.7	-1.5	0.02654
81	Q96IJ6	GMPPA	GDP-mannose pyrophosphorylase A	0.7	-1.5	0.02541
82	O14908	GIPC1	GIPC PDZ domain containing family member 1	1.8	1.8	0.00449
83	Q06210	GFPT1	glutamine--fructose-6-phosphate transaminase 1	0.7	-1.5	0.00580
84	Q9UJY5	GGA1	golgi associated, gamma adaptin ear containing, ARF binding protein 1	1.8	1.8	0.01535
85	Q9H8Y8	GORASP2	golgi reassembly stacking protein 2	1.3	1.3	0.02927
86	Q9Y450	HBS1L	HBS1 like translational GTPase	0.8	-1.3	0.02742
87	P14625	HSP90B1	heat shock protein 90 beta family member 1	0.5	-1.9	0.00990
88	P02100	HBE1	hemoglobin subunit epsilon 1	6.0	6.0	0.00130
89	P05114	HMGN1	high mobility group nucleosome binding domain 1	2.4	2.4	0.02945
90	Q71DI3	HIST2H3C	histone cluster 2 H3 family member c	2.0	2.0	0.02183
91	Q9UBN7	HDAC6	histone deacetylase 6	0.6	-1.5	0.02763
92	P08397	HMBS	hydroxymethylbilane synthase	3.4	3.4	0.02439
93	Q8NBQ5	HSD17B11	hydroxysteroid 17-beta dehydrogenase 11	0.6	-1.7	0.02828
94	P12268	IMPDH2	inosine monophosphate dehydrogenase 2	0.6	-1.7	0.02500
95	Q9H1B7	IRF2BPL	interferon regulatory factor 2 binding protein like	2.0	2.0	0.03020
96	Q9ULR0	ISY1	ISY1 splicing factor homolog	1.5	1.5	0.00262
97	O00629	KPNA4	karyopherin subunit alpha 4	1.5	1.5	0.00094
98	Q92945	KHSRP	KH-type splicing regulatory protein	1.7	1.7	0.00005
99	Q8TCG1	KIAA1524	KIAA1524	31.6	31.6	1.08e-11
100	Q96EK9	KTI12	KTI12 chromatin associated homolog	1.6	1.6	0.02983
101	Q16773	KYAT1	kynurenine aminotransferase 1	0.7	-1.4	0.00118
102	P20700	LMNB1	lamin B1	1.9	1.9	0.00421
103	P49257	LMAN1	lectin, mannose binding 1	1.3	1.3	0.00521
104	P09960	LTA4H	leukotriene A4 hydrolase	0.7	-1.5	0.01257
105	P48163	ME1	malic enzyme 1	1.3	1.3	0.02611
106	P34949	MPI	mannose phosphate isomerase	0.6	-1.8	0.01273
107	O95983	MBD3	methyl-CpG binding domain protein 3	1.4	1.4	0.01772
108	Q96E11	MRRF	mitochondrial ribosome recycling factor	0.8	-1.3	0.01737
109	P27361	MAPK3	mitogen-activated protein kinase 3	0.8	-1.3	0.00357

110	P36507	MAP2K2	mitogen-activated protein kinase kinase 2	0.7	-1.4	0.01051
111	Q8NI22	MCFD2	multiple coagulation factor deficiency 2	0.6	-1.6	0.02722
112	Q96EY5	MVB12A	multivesicular body subunit 12A	0.6	-1.7	0.00311
113	P43246	MSH2	mutS homolog 2	0.7	-1.4	0.02085
114	P35579	MYH9	myosin heavy chain 9	1.9	1.9	0.00076
115	P16083	NQO2	NAD(P)H quinone dehydrogenase 2	0.6	-1.7	0.00366
116	O95182	NDUFA7	NADH:ubiquinone oxidoreductase subunit A7	1.5	1.5	0.00673
117	Q16795	NDUFA9	NADH:ubiquinone oxidoreductase subunit A9	1.8	1.8	0.01332
118	Q9H3P2	NELFA	negative elongation factor complex member A	1.3	1.3	0.00477
119	Q8NEJ9	NGDN	neuroguidin	1.6	1.6	0.01186
120	Q9ULX3	NOB1	NIN1/PSMD8 binding protein 1 homolog	1.4	1.4	0.00801
121	P78316	NOP14	NOP14 nuc+D2:D251leolar protein	1.6	1.6	0.00387
122	Q9Y3C1	NOP16	NOP16 nucleolar protein	1.4	1.4	0.02037
123	Q08J23	NSUN2	NOP2/Sun RNA methyltransferase family member 2	1.6	1.6	0.02112
124	Q9UKX7	NUP50	nucleoporin 50	2.8	2.8	8.09e-9
125	P53384	NUBP1	nucleotide binding protein 1	0.5	-1.9	0.00099
126	O60313	OPA1	OPA1, mitochondrial dynamin like GTPase	0.8	-1.3	0.00959
127	Q96FW1	OTUB1	OTU deubiquitinase, ubiquitin aldehyde binding 1	0.6	-1.7	0.00922
128	O95747	OXSR1	oxidative stress responsive 1	0.6	-1.6	0.00796
129	Q10713	PMPCA	peptidase, mitochondrial processing alpha subunit	0.7	-1.4	0.01229
130	Q6GMV3	PTRHD1	peptidyl-tRNA hydrolase domain containing 1	0.6	-1.7	0.00742
131	O60664	PLIN3	perilipin 3	0.5	-2.2	0.00417
132	P30048	PRDX3	peroxiredoxin 3	0.6	-1.7	0.01195
133	P49585	PCYT1A	phosphate cytidylyltransferase 1, choline, alpha	1.5	1.5	0.00030
134	Q01813	PFKP	phosphofructokinase, platelet	0.3	-2.9	0.00034
135	P52209	PGD	phosphogluconate dehydrogenase	0.7	-1.3	0.02385
136	P11908	PRPS2	phosphoribosyl pyrophosphate synthetase 2	0.8	-1.3	0.01686
137	P11216	PYGB	phosphorylase, glycogen; brain	0.6	-1.5	0.02994
138	P78330	PSPH	phosphoserine phosphatase	0.7	-1.5	0.02233
139	P53801	PTTG1IP	pituitary tumor-transforming 1 interacting protein	1.8	1.8	0.00011
140	Q9Y446	PKP3	plakophilin 3	1.5	1.5	0.00579
141	O43242	PSMD3	proteasome 26S subunit, non-ATPase 3	1.7	1.7	0.02593
142	Q15008	PSMD6	proteasome 26S subunit, non-ATPase 6	1.7	1.7	0.00173
143	Q9UL46	PSME2	proteasome activator subunit 2	0.5	-2.0	0.01916
144	P20618	PSMB1	proteasome subunit beta 1	0.6	-1.6	0.00108
145	O14744	PRMT5	protein arginine methyltransferase 5	0.7	-1.5	0.00374
146	P30101	PDIA3	protein disulfide isomerase family A member 3	0.4	-2.5	0.00109
147	Q15084	PDIA6	protein disulfide isomerase family A member 6	0.5	-2.0	0.02041
148	Q13131	PRKAA1	protein kinase AMP-activated	0.7	-1.4	0.00034

			catalytic subunit alpha 1			
149	P54619	PRKAG1	protein kinase AMP-activated non-catalytic subunit gamma 1	0.8	-1.3	0.01902
150	P62140	PPP1CB	protein phosphatase 1 catalytic subunit beta	0.7	-1.4	0.02243
151	O14974	PPP1R12A	protein phosphatase 1 regulatory subunit 12A	0.6	-1.6	0.00178
152	Q15172	PPP2R5A	protein phosphatase 2 regulatory subunit B'alpha	0.6	-1.5	0.00791
153	P30154	PPP2R1B	protein phosphatase 2 scaffold subunit Abeta	0.5	-1.9	0.02214
154	Q9Y570	PPME1	protein phosphatase methylesterase 1	1.3	1.3	0.03073
155	Q86TP1	PRUNE1	prune exopolyphosphatase	0.6	-1.6	0.02140
156	Q08623	PUDP	pseudouridine 5'-phosphatase	0.6	-1.7	0.01141
157	Q9NVS9	PNPO	pyridoxamine 5'-phosphate oxidase	0.8	-1.2	0.02008
158	P30613	PKLR	pyruvate kinase, liver and RBC	2.6	2.6	0.00054
159	P14618	PKM	pyruvate kinase, muscle	1.7	1.7	0.01963
160	Q9UL25	RAB21	RAB21, member RAS oncogene family	0.7	-1.4	0.00572
161	P51149	RAB7A	RAB7A, member RAS oncogene family	1.6	1.6	0.00014
162	Q15293	RCN1	reticulocalbin 1	0.7	-1.5	0.01503
163	P13489	RNH1	ribonuclease/angiogenin inhibitor 1	0.6	-1.6	0.02427
164	P23921	RRM1	ribonucleotide reductase catalytic subunit M1	0.6	-1.6	0.00854
165	P47914	RPL29	ribosomal protein L29	1.4	1.4	0.01476
166	P62249	RPS16	ribosomal protein S16	1.6	1.6	0.03079
167	Q5JTH9	RRP12	ribosomal RNA processing 12 homolog	1.7	1.7	0.00767
168	Q9P2E9	RRBP1	ribosome binding protein 1	0.6	-1.7	0.00081
169	Q9BTD8	RBM42	RNA binding motif protein 42	1.3	1.3	0.00699
170	Q9Y3B8	REXO2	RNA exonuclease 2	2.1	2.1	0.00276
171	O15160	POLR1C	RNA polymerase I subunit C	1.3	1.3	0.01159
172	O14802	POLR3A	RNA polymerase III subunit A	1.5	1.5	0.02573
173	Q9BUI4	POLR3C	RNA polymerase III subunit C	1.4	1.4	0.01835
174	Q6R327	RICTOR	RPTOR independent companion of MTOR complex 2	0.9	-1.1	0.00649
175	O94901	SUN1	Sad1 and UNC84 domain containing 1	1.5	1.5	0.00293
176	Q9NSI8	SAMSN1	SAM domain, SH3 domain and nuclear localization signals 1	1.9	1.9	0.02554
177	Q15436	SEC23A	Sec23 homolog A, coat complex II component	0.7	-1.4	0.02542
178	P53992	SEC24C	SEC24 homolog C, COPII coat complex component	0.6	-1.6	0.02093
179	Q16181	SEPT7	septin 7	0.8	-1.3	0.01129
180	Q96GA7	SDSL	serine dehydratase like	0.7	-1.5	0.01394
181	Q99961	SH3GL1	SH3 domain containing GRB2 like 1, endophilin A2	1.3	1.3	0.03055
182	Q9BWW4	SSBP3	single stranded DNA binding protein 3	1.9	1.9	0.01116
183	O43765	SGTA	small glutamine rich tetratricopeptide repeat containing alpha	0.7	-1.4	0.01338
184	P08579	SNRPB2	small nuclear ribonucleoprotein polypeptide B2	0.8	-1.2	0.00531
185	P62308	SNRPG	small nuclear ribonucleoprotein polypeptide G	1.4	1.4	0.00383
186	P14678	SNRPB	small nuclear ribonucleoprotein	1.3	1.3	0.02297

			polypeptides B and B1			
187	P11166	SLC2A1	solute carrier family 2 member 1	2.0	2.0	0.00073
188	P11169	SLC2A3	solute carrier family 2 member 3	2.4	2.4	0.00087
189	Q9Y6M7	SLC4A7	solute carrier family 4 member 7	0.8	-1.3	0.02290
190	Q96SB4	SRPK1	SRSF protein kinase 1	1.4	1.4	0.01642
191	Q9BRK5	SDF4	stromal cell derived factor 4	0.7	-1.4	0.00207
192	Q13586	STIM1	stromal interaction molecule 1	1.2	1.2	0.01705
193	P04179	SOD2	superoxide dismutase 2, mitochondrial	0.6	-1.6	0.00688
194	Q8IYB8	SUPV3L1	Suv3 like RNA helicase	1.4	1.4	0.00859
195	Q96A49	SYAP1	synapse associated protein 1	0.9	-1.1	0.02492
196	Q9Y490	TLN1	talin 1	0.5	-1.8	0.00969
197	P17987	TCP1	t-complex 1	0.6	-1.6	0.02344
198	O43156	TTI1	TELO2 interacting protein 1	1.4	1.4	0.02114
199	Q6NXR4	TTI2	TELO2 interacting protein 2	1.5	1.5	0.01511
200	Q9Y4R8	TELO2	telomere maintenance 2	1.5	1.5	0.00220
201	O95881	TXNDC12	thioredoxin domain containing 12	0.5	-1.9	0.02849
202	P04818	TYMS	thymidylate synthetase	1.5	1.5	0.02532
203	Q9H0E2	TOLLIP	toll interacting protein	1.3	1.3	0.00458
204	Q99598	TSNAX	translin associated factor X	0.7	-1.4	0.01486
205	Q9BTV4	TMEM43	transmembrane protein 43	2.1	2.1	0.01475
206	O14787	TNPO2	transportin 2	2.6	2.6	0.00002
207	Q9UPN9	TRIM33	tripartite motif containing 33	1.1	1.1	0.01969
208	Q6IBS0	TWF2	twinfilin actin binding protein 2	0.8	-1.3	0.02241
209	P26368	U2AF2	U2 small nuclear RNA auxiliary factor 2	1.4	1.4	0.02666
210	Q9NRR5	UBQLN4	ubiquilin 4	0.6	-1.8	0.00154
211	Q5T6F2	UBAP2	ubiquitin associated protein 2	1.3	1.3	0.02035
212	Q14157	UBAP2L	ubiquitin associated protein 2 like	0.6	-1.6	0.00643
213	P22314	UBA1	ubiquitin like modifier activating enzyme 1	0.5	-2.0	0.00240
214	O94966	USP19	ubiquitin specific peptidase 19	0.6	-1.6	0.00673
215	Q86UV5	USP48	ubiquitin specific peptidase 48	0.6	-1.8	0.00613
216	P45974	USP5	ubiquitin specific peptidase 5	1.4	1.4	0.01126
217	Q9NYU2	UGGT1	UDP-glucose glycoprotein glucosyltransferase 1	0.6	-1.6	0.00753
218	Q9HAU5	yeast	UPF2 regulator of nonsense transcripts homolog	1.4	1.4	0.02109
219	O60287	URB1	URB1 ribosome biogenesis 1 homolog	1.4	1.4	0.02046
220	O75691	UTP20	UTP20, small subunit processome component	1.4	1.4	0.02863
221	Q9Y277	VDAC3	voltage dependent anion channel 3	1.3	1.3	0.01835
222	Q9P253	VPS18	VPS18, CORVET/HOPS core subunit	1.3	1.3	0.02611
223	O15213	WDR46	WD repeat domain 46	1.2	1.2	0.02588
224	Q9Y2W2	WBP11	WW domain binding protein 11	1.3	1.3	0.01160
225	Q9HCS7	XAB2	XPA binding protein 2	1.5	1.5	0.01598
226	Q86WB0	ZC3HC1	zinc finger C3HC-type containing 1	0.8	-1.3	0.00882
227	Q9Y4E5	ZNF451	zinc finger protein 451	0.6	-1.7	0.02582
228	Q14966	ZNF638	zinc finger protein 638	0.7	-1.5	0.02758
229	O75312	ZPR1	ZPR1 zinc finger	0.7	-1.5	0.00236